Space Sci Rev
DOI 10.1007/s11214-010-9636-0

Implications of Rotation, Orbital States, Energy Sources, and Heat Transport for Internal Processes in Icy Satellites

Hauke Hussmann · Gaël Choblet · Valéry Lainey · Dennis L. Matson · Christophe Sotin · Gabriel Tobie · Tim Van Hoolst

Received: 13 May 2009 / Accepted: 8 February 2010

Abstract Internal processes in icy satellites, e.g. the exchange of material from the subsurface to the surface or processes leading to volcanism and resurfacing events, are a consequence of the amount of energy available in the satellites' interiors. The latter is mainly determined shortly after accretion by the amount of radioactive isotopes incorporated in the silicates during the accretion process. However, for satellites—as opposed to single objects—important contributions to the energy budget on long time-scales can come from the interaction with other satellites (forcing of eccentricities of satellites in resonance) and consequently from the tidal interaction with the primary planet. Tidal evolution involves both changes of the rotation state—usually leading to the 1:1 spin orbit coupling—and long-term variations of the satellite orbits. Both processes are dissipative and thus connected with heat production in the interior. The way heat is transported from the interior to the surface (convection, conduction, (cryo-) volcanism) is a second main aspect that determines how internal processes in satellites work. In this chapter we will discuss the physics of heat production and heat transport as well as the rotational and orbital states of satellites. The

H. Hussmann (✉)
DLR Institute of Planetary Research, Rutherfordstr. 2, 12489 Berlin, Germany
e-mail: hauke.hussmann@dlr.de

G. Choblet · G. Tobie
Laboratoire de Planétologie et Géodynamique, Université de Nantes, 2, rue de la houssinière, BP 92208, 44322 Nantes, France

V. Lainey
Institut de Mécanique Céleste et de Calcul des Éphémérides (IMCCE), Observatoire de Paris 77, Avenue Denfert-Rochereau, 75014 Paris, France

D.L. Matson · C. Sotin
Jet Propulsion Laboratory/California Institute of Technology, 4800 Oak Grove Drive, Pasadena, CA 91109, USA

T. Van Hoolst
Royal Observatory of Belgium, Ringlaan 3, 1180 Brussels, Belgium

Published online: 17 March 2010

relevance of the different heat sources for the moons in the outer solar system are compared and discussed.

Keywords Satellites · Energy sources · Rotation · Tides · Orbital dynamics · Heat transfer

1 Introduction

The first evidence that dynamical processes play a significant role for the evolution and present states of satellites in the outer solar system was obtained in the 1970s when ground-based observations revealed an anomalous output of thermal emission and unusual spectral reflectance at the surface of Io, the innermost of the Galilean Satellites of Jupiter. Additionally, the existence of Io's ion and neutral gas clouds and plasma torus were detected at that time (Nash et al. 1986, and references therein). Dynamical variations—"outbursts"—in Io's infrared spectra (Witteborn et al. 1979) were first recognized shortly before the *Voyager 1* encounter in 1979. The *Voyager 1* flyby revealed Io's intense geologic activity and vigorous volcanism (Smith et al. 1979), confirming the presence of enormous internal energy sources that had been theoretically predicted by Peale et al. (1979) shortly before the encounter. Io is an excellent example showing that internal energy sources can be closely connected to a satellite's orbital state, here its orbital eccentricity and its tidal interaction with the primary planet. Additionally, the importance of mean motion resonances forcing the eccentricities of satellites was recognized at that time as an essential part of the energy available within moons evolving in satellite systems (Yoder 1979). Tidal friction has been recognized as the main heat source in Io's interior giving rise to the thermal and volcanic activity observed by the *Galileo* mission (Geissler 2003; McEwen et al. 2004), by recent ground-based campaigns (Marchis et al. 2005) and by the *New Horizons* fly-by of the Jupiter system in 2007 on its way to Pluto (Spencer et al. 2007).

With the observation of anomalously high surface temperatures and large eruptions of water-vapor and dust from the icy surface of the Saturnian satellite Enceladus, the *Cassini* spacecraft detected strong internal activity of a relatively small icy moon ($R = 252$ km) in the outer solar system (Porco et al. 2006; Spencer et al. 2006). Enceladus' activity presumably implies liquid water and high temperatures within the moon's ice shell. However, the processes generating such a locally confined activity are still debated. Especially, with the presence of liquid water tidal dissipation can be considered as the major heat source.

During the flyby of *Voyager 2* at Neptune's moon Triton the imaging data showed plumes rising in the satellites' tenuous atmosphere (Soderblom et al. 1990). However, the energy involved in this kind of activity is considerably smaller as compared to the eruptions on Io and Enceladus. It is not clear whether Triton's activity is related to internal processes or merely a consequence of solar insolation (Brown et al. 1990).

So far Io, Enceladus and Triton are the only satellites of the solar system showing present-day activity on their surfaces.[1] However, there is ample evidence of past activity on icy moons which is related to intense heating and exchange of energy in their interiors. Io, Europa, Ganymede, Enceladus, Titan, Dione, Miranda, Ariel, and Triton show signs of substantial resurfacing on global scales. Iapetus, Titania, Tethys and Rhea display regional terrain characterized by tectonism and/or other geological processes that occurred early in their histories. In contrast Callisto, Mimas, Oberon and Umbriel did not pass through active periods

[1] Titan's surface is currently modified by interaction with its dense atmosphere. Since we focus on processes related to the interior of the moons this kind of resurfacing is not discussed here.

in their histories, as indicated by their heavily cratered surfaces. These examples show that activity in icy satellites is not a simple consequence of their mass, size, composition, or semi-major axis. On the basis of the satellites' bulk properties the state of activity—be it early or late in their histories—is unpredictable. It is rather a consequence of the satellites properties in combination with external influence, e.g., impacts or gravitational interaction with other bodies. Early activity may be linked to non-synchronous rotation during early epochs before the 1:1 spin-orbit coupling, which is the current state occupied by all large satellites, was established. During that early epoch large impacts may have significantly contributed to the energy budget of the moons. Later, orbital resonances and tidal heating in the synchronous state in elliptical orbits have played an important role for some of the satellites.

Earlier reviews on orbital and rotational states are given by Peale (1986) and on the thermal evolution and convection by Schubert et al. (1986) and McKinnon (1998).

In this chapter we discuss the significance of energy sources that are available for the satellites and the internal processes that can be triggered during their evolution. This requires a description of their rotational and dynamical states, as well as their composition and state of differentiation. The connection from energy sources to dynamical processes is provided by heat transport mechanisms finally releasing energy at the surface. The available energy sources and their relevance for internal processes and satellite evolution are compared for the individual objects.

2 Rotation

The large and medium-sized (radius > 200 km) satellites of the Solar System all have rotation periods that are almost exactly equal to their revolution periods. Non-synchronous rotation might occur for some satellites. The typical time-scale of 10^4–10^5 years for non-synchronous rotation, however, significantly exceeds the periods of revolution, of the order of days or tens of days. The state of synchronous rotation is stable due to the asymmetric mass distribution with the longest axis pointing towards the central planet at pericenter (Goldreich and Peale 1966, see also Sect. 3.2.2). However, stability does not imply that the rotation rate is constant. Both internal and external forces may cause the rotation rate to vary about its equilibrium value. In particular, due to the eccentricity of all the satellite orbits, the long axis is not pointing toward the central planet but approximately in the direction to the empty focus of the orbit (Murray and Dermott 1999) so that the central planet exerts a time-variable gravitational torque on the satellite. As a result, the satellite periodically varies its rotation rate about the mean rate and the direction of the long axis librates with respect to its orientation at constant mean rotation rate (forced libration). As is well known for the Earth, the rotation rate of a celestial body can also vary as a result of angular momentum exchange between the atmosphere and the solid body. These variations may have been observed for Titan (Stiles et al 2008, 2010).

Observations of librations provide information on the moments of inertia of the satellite since the gravitational torque exerted by the central planet is proportional to the difference between moments of inertia and the rotational reaction depends on the moment of inertia about the rotation axis. Therefore, together with measurements of the gravitational field, rotation can be used to determine the degree of differentiation of a satellite. Moreover, a subsurface ocean strongly affects the rotation variations and leads to a transfer of angular momentum and energy between the solid and liquid layers. Rotation observations could prove the existence of an internal ocean and could even constrain the thickness of the overlying ice shell. Besides providing constraints on the interior structure, librations can also increase the tidal heating rate of a satellite (e.g., Wisdom 2004).

2.1 Static Tides and Shape

Rotation flattens a synchronously rotating satellite at its poles and creates an equatorial bulge, whereas the static tides stretch the satellite in the direction to the central planet and cause a contraction in the direction perpendicular to it. As a result, the longest axis is expected to be along the planet-satellite line at pericenter and the short axis is parallel to the rotation axis. For a satellite in hydrostatic equilibrium, rotation and static tides are the only causes of deviations from spherical symmetry and the satellite's shape can be calculated by applying Clairaut theory (see, e.g. Jeffreys 1952; Hubbard 1984; Moritz 1990). In view of the study of variations in the rotation speed of satellites, the difference between the long and short axes of the equator is dynamically important. For a given spherical reference model of the interior structure with density profile $\rho(r_0)$, where r_0 is the radial coordinate from the center of the model, the equatorial flattening β of the model due to the static tides raised by the central planet can be determined from Clairaut's second-order differential equation

$$\frac{d^2\beta}{dr_0^2} + \frac{6}{r_0}\frac{\rho}{\overline{\rho}}\frac{d\beta}{dr_0} - \frac{6}{r_0^2}\left(1 - \frac{\rho}{\overline{\rho}}\right)\beta = 0, \tag{1}$$

and the associated boundary condition

$$\frac{d\beta}{dr_0}(R) = \frac{1}{R}\left[\frac{15}{2}q - 2\beta(R)\right] \tag{2}$$

(e.g. Hubbard 1984; Van Hoolst et al. 2008). Here, R is the mean radius, $q = (n^2R^3)/(Gm_s)$ the ratio of the centrifugal acceleration to the gravitational acceleration, and m_s the total mass of the satellite; $\overline{\rho}$ is the mean density in a sphere of radius r_0 and n the orbital mean motion. The flattening $\beta(r_0) = [a(r_0) - b(r_0)]/a(r_0)$, where $a(r_0) > b(r_0)$ are the lengths of the two principal axes in the equatorial plane of the ellipsoidal surface with mean radius r_0.

Instead of the difference in length of the long and short equatorial axes, the equatorial moment of inertia difference $B - A$ is dynamically more relevant and can be calculated by integration over the radial coordinate:

$$B - A = \frac{8\pi}{15}\int_0^R \rho(r_0')\frac{d(\beta r_0'^5)}{dr_0'}dr_0'. \tag{3}$$

Data on the geometric shape and on the gravitationally determined moment of inertia difference are available for a selection of satellites. The shape of many but not all large and medium-sized satellites seems to be consistent to first order with that of a relaxed satellite in hydrostatic equilibrium (e.g. Thomas et al. 2007; Van Hoolst et al. 2008, 2009). A necessary but not sufficient condition for hydrostatic equilibrium is that the ratio J_2/C_{22} of the degree two coefficients of the gravitational field is equal to 10/3. At least two different close flybys—one equatorial and one polar—are required to test this hypothesis. So far, Io is (apart from the Moon) the only satellite for which polar and equatorial flybys could be used. The hydrostatic assumption was found to be consistent with the gravity data analysis from these flybys (Schubert et al. 2004). Data from one polar and three equatorial passes was also obtained at Ganymede. The independent determination of J_2 and C_{22} was, however, impossible. Detailed analysis suggests the presence of mass anomalies inside Ganymede that may be related to the different rock content of Ganymede's dark and bright terrain (Schubert et al. 2004; Palguta et al. 2009).

The shape of Saturn's satellite Iapetus is remarkable. It corresponds to a body in hydrostatic equilibrium that rotates with a period of about 16 h (Thomas et al. 2007), much faster than at its current period of 79.33 days. This implies that its shape has been conserved from a much faster spin-state early in its evolution (for details see Schubert et al. 2010, this issue).

2.2 Libration

2.2.1 Librations of a Rigid Body

Since satellite orbits are eccentric (eccentricity between about 0.001 and 0.03 for the large and medium-sized satellites), the orbital speed is variable and satellites do not always show exactly the same face to their central planet. As a consequence, the central planet exerts a time-variable gravitational torque on the satellite that tends to modify the satellite's rotation rate. Longitudinal librations are the corresponding changes in the rotation angle. If a satellite can be assumed to respond as a rigid body to an external gravitational force, conservation of angular momentum $H = C\dot{\theta}$, where C is the largest (polar) principal moment of inertia and θ the angle of rotation between the long axis of the satellite and the major axis of the orbit, can be expressed as (e.g. Goldreich and Peale 1966)

$$C\ddot{\theta} + \frac{3}{2}n^2(B-A)\left(\frac{a}{r}\right)^3 \sin 2(\theta - f) = 0, \tag{4}$$

where the second term is equal and opposite to the gravitational torque of the central planet on the satellite and zero obliquity is assumed. Here, a is the semi-major axis, f the true anomaly, and r the distance between the centers of mass of the central planet and the satellite. The rigid rotational response is a good approximation for an entirely solid satellite without internal ocean since the effect of elastic deformation on the moment of inertia of the satellite is small (Van Hoolst et al. 2008).

It is convenient to introduce the small libration angle $\gamma = \theta - M$ and expand the equations as a series in mean anomaly M and eccentricity e by using well-known expansions for $(a/r)^3$, $\cos f$, and $\sin f$ (Cayley 1861). After linearization of (4) in eccentricity and libration angle, we then have

$$C\ddot{\gamma} + 3n^2(B-A)\gamma = 6en^2(B-A)\sin M. \tag{5}$$

The right-hand side causes the satellite to librate with a period equal to the orbital period of the satellite and amplitude (e.g., Murray and Dermott 1999)

$$A_\gamma = \frac{2\omega_f^2 e}{n^2 - \omega_f^2}. \tag{6}$$

The natural free frequency ω_f follows directly from the left-hand side of (5) (e.g., Comstock and Bills 2003):

$$\omega_f = n\sqrt{\frac{3(B-A)}{C}}. \tag{7}$$

It is orders of magnitude smaller than the mean motion n since $B - A$ is much smaller than C. Therefore, the amplitude of the forced libration can be approximated by (Eckhardt 1981)

$$A_\gamma = 6\frac{B-A}{C}e. \tag{8}$$

Dissipation processes due to tides and libration damp the long-periodic free libration, so that it can be assumed to have a (almost) zero amplitude. Comstock and Bills (2003) provide a survey of libration amplitudes of satellites calculated by assuming that the relative moment of inertia difference $(B - A)/C$ corresponds to that of a homogeneous body in hydrostatic equilibrium. Both assumptions could lead to errors of the order of some ten percent for the larger and rapidly rotating satellites (e.g., Van Hoolst et al. 2008 in application to Europa) or even larger for bodies that have a strong non-hydrostatic contribution to their flattening. Typical maximum displacements of the long axis with respect to its equilibrium position at the surface range from a few tens to a few hundreds of meters. The largest amplitude is expected for Mimas (about 1.4 km) and for the non-synchronous rotator Hyperion (about 1.3 km) (Comstock and Bills 2003).

For small deviations from a spherically symmetric shape the relative contribution of the forced libration to tidal heating of a synchronous satellite is of the order of $3(B - A)/C$ (Wisdom 2004). This ratio is smaller than 0.01 for the large satellites but of the order of 0.1 for more aspherical satellites like Mimas, Enceladus, and Tethys (Thomas et al. 2007). A resonance between the orbital frequency and the free libration frequency could further enhance the heating (Wisdom 2004).

2.2.2 *Effect of a Subsurface Ocean*

When a subsurface ocean exists, the rotation variations of the ice shell can be different from those of the interior. It is tempting to assume that the shell is dynamically decoupled from the interior by the ocean, but pressure and gravitational forces between the shell, ocean, and solid interior are likely to be efficient in coupling the rotational motion of the shell to that of the solid interior (Van Hoolst et al. 2008, 2009). Internal gravitational and pressure coupling arises when the principal axes of the shell are not aligned with those of the interior, for example as a result of the different rotational response of the shell and interior to the gravitational torque of the central planet. As a result of internal coupling, energy and angular momentum are exchanged between the internal layers.

Friction on the boundaries of an internal ocean can be neglected because of the small ocean viscosity, provided that variations in ocean-floor topography are small. Furthermore, electromagnetic coupling between the ocean and the shell and between the ocean and the interior is not considered to be important, at least not when the satellite is lacking a self-generated magnetic field. By assuming that the ocean dynamics can be expressed essentially as a small rigid rotation and by neglecting topography on the ellipsoidal boundaries between the interior, the ocean, and the shell, Van Hoolst et al. (2009) showed that the existence of a subsurface ocean increases the amplitude of the forced librations. For example, for a highly differentiated model of Titan with a 224 km thick ammonia–water ocean beneath an ice shell of 69 km thickness (Sohl et al. 2003), the amplitude of libration equals 1.5×10^{-4} rad, whereas in the rigid assumption, the amplitude is only 1.7×10^{-5} rad (Van Hoolst et al. 2009). These values are calculated by assuming a hydrostatic flattening profile. In that case the libration amplitude increases about linearly with decreasing shell thickness (Van Hoolst et al. 2008), offering the possibility to determine the thickness of the ice shell from libration observations. For thin shells, for example a few km for Europa, the forced libration can become resonantly enhanced due to a resonance with a natural mode of the satellite. This mode is essentially a free libration of the ice shell and its eigenfrequency increases with decreasing moment of inertia of the shell C_s (Van Hoolst et al. 2008). Because the librations are larger when a satellite has a subsurface ocean, tidal heating is expected to increase with respect to heating for a completely solid body. Moreover, the relative rotation of a viscous ocean with respect to the solid boundaries could be an additional heat source.

2.3 Length-of-Day Variations of Titan

Cassini radar observations show that Titan's spin is slightly faster than synchronous leading to a shift of 0.12° per year in apparent longitude (Stiles et al. 2010). It is thought that long-periodic exchanges of angular momentum between Titan's surface and atmosphere cause the orientation of Titan to vary with an amplitude of about 0.005 rad. Periodic length-of-day (LOD) variations with main period of 14.74 yrs were predicted by Tokano and Neubauer (2005) on the basis of their general circulation model of the atmosphere. For a solid Titan, their predicted amplitude is smaller than the observed value. If Titan has an ocean and the rotation of the shell could be considered decoupled from the interior, the atmosphere would only force rotation variations of the shell and the amplitude of the surface rotation variations would be the observed value (Tokano and Neubauer 2005). However, misalignment of the long axis of Titan with the direction to Saturn due to the atmosphere results in a strong gravitational restoring torque of Saturn exerted on Titan, which limits the amplitude of the orientation variations to a value of about 10^{-4} rad, or about 50 times smaller than observations indicate (Van Hoolst et al. 2009). Although this suggests that Titan cannot be entirely solid, the combined effect of the gravitational torque due to Saturn and internal coupling when a subsurface ocean exists in Titan also strongly reduces the rotation variations with respect to that for a decoupled shell. By assuming hydrostatic flattening and taking into account the atmospheric torque predicted by Tokano and Neubauer (2005), the rotation variations for Titan with an internal ocean can be shown to be about as small as expected for an entirely solid Titan. Internal coupling contributes to reducing the amplitude of the rotation variations by its tendency to lock the rotation of the shell to that of the interior (Karatekin et al. 2008). Besides the much smaller predicted than observed LOD variations, Saturn's torque is also predicted to cause the rotation to be slower than synchronous in contrast to the Cassini observations. These large differences with the observations in amplitude and in phase suggest that non-hydrostatic effects in Titan are important. In particular, if non-hydrostatic effects would strongly reduce the equatorial flattening of the ice shell above an internal ocean, the amplitude and phase of the calculated rotation variations were similar to the observed values. Alternatively, the calculated LOD variations would increase if the atmospheric torque was larger than predicted or if fast viscous relaxation of the ice shell would reduce the gravitational coupling (Van Hoolst and Karatekin 2008). However, it remains to be studied whether an almost two order of magnitude increase is possible and if these effects can also explain the phase difference of the predicted rotation variations. On the other hand, Noyelles (2008) suggests that a resonantly excited long period wobble could explain the apparent faster rotation even for an entirely solid Titan, which would nevertheless require fine-tuning of Titan's moment of inertia.

3 Orbital Dynamics

3.1 Resonances Among Satellites

Many satellites in the Solar system are locked in resonance. An orbital resonant state occurs when a linear combination of orbital frequencies is zero on average. Such configurations can be a consequence of expansion or regression of the orbits under tidal interactions. However, a primordial origin as suggested by e.g., Peale and Lee (2002) for the Galilean satellites would be an alternative scenario for the formation of resonances.

When satellites are in a resonant state they exchange their orbital energy and angular momentum. The computation of orbital variations induced by tidal effects is then rendered

more complex by the mutual gravitational interaction of the moons in resonance. For the main satellites of the giant planets, several resonances are observed. With L being the mean longitude, Ω the longitude of the node and ϖ the longitude of the periapsis, the following resonances and their respective arguments are observed in the Saturnian system:

(i) Mimas (subscript M) and Tethys (T)

$$4L_{\mathrm{T}} - 2L_{\mathrm{M}} - \Omega_{\mathrm{T}} - \Omega_{\mathrm{M}} = \phi; \tag{9}$$

conjunctions librate about ϕ, the midpoint of the node (amplitude 43.6° and period 71.8 years) (Murray and Dermott 1999);

(ii) Enceladus (subscript E) and Dione (D)

$$L_{\mathrm{E}} - 2L_{\mathrm{D}} + \varpi_{\mathrm{E}} = 0, \tag{10}$$

with a libration amplitude of 0.297° and a period of 11.1 years (Murray and Dermott 1999);

(iii) Titan (subscript T) and Hyperion (H)

$$3L_{\mathrm{T}} - 4L_{\mathrm{H}} + \varpi_{\mathrm{H}} = \pi, \tag{11}$$

with libration amplitude of 36° over a 640 days period.

The three inner Galilean satellites (Io (I), Europa (E), and Ganymede (G)) are locked in the Laplace resonance (who first demonstrated the stability of this configuration) and satisfies the longitude relation

$$L_{\mathrm{I}} - 3L_{\mathrm{E}} + 2L_{\mathrm{G}} = \pi, \tag{12}$$

with a small amplitude of 0.175° over a 2059.6 days period (Lainey et al. 2006). No orbital resonances are known among the main Uranian satellites.

The main aspect of resonances for satellite evolution is the forcing of eccentricities (e-type resonance) and inclinations (i-type resonance). For satellites, locked in an e-type resonance the forced eccentricities are maintained, although dissipation within the satellites tends to reduce them. This can keep tidal heating ongoing on geological timescales. The forced eccentricities and inclinations, associated with the resonances above are given in Table 1.

3.2 Orbital Variation Due to Tides

Tidal effects arise because of the differences in gravitational attraction due to an external mass experienced on different parts of a body. This gives rise to tidal bulges that are directed toward the tide-raising body, if no dissipation occurs. Because most satellites are in a 1:1 spin orbit resonance, it is convenient to separately consider the tidal effects in the planet and in the satellite.

3.2.1 Tides Raised in the Planet

If no dissipation occurs in the planet, the tidal bulge would be perfectly aligned with the planet–satellite line. Because of tidal dissipation inside the primary, a phase lag arises and leads to an exchange of angular momentum between the spin of the planet and the orbit of

Table 1 Forced eccentricities and inclinations of satellites in resonance (e.g., Murray and Dermott 1999). The eccentricity of Europa is forced due to two resonances. The perturbations by Enceladus and Hyperion are too small to significantly force the eccentricities of Dione and Titan, respectively. Titan has a large free eccentricity of 0.0292. Also in the cases of Ganymede and Dione the free eccentricities of 0.0015 and 0.0022, respectively (Peale 1986), significantly exceed the forced eccentricities

Satellite	Ratio of mean motions	e (forced)	i (forced)
Io	2:1 Io–Europa	0.0041	–
Europa	2:1 Io–Europa and 2:1 Europa–Ganymede	0.0101	–
Ganymede	2:1 Europa–Ganymede	0.0006	–
Enceladus	2:1 Enceladus–Dione	0.0044	–
Dione	2:1 Enceladus–Dione	$\approx 10^{-5}$	–
Mimas	4:2 Mimas–Tethys	–	1.53°
Tethys	4:2 Mimas–Tethys	–	1.09°
Titan	4:3 Titan–Hyperion	–	–
Hyperion	4:3 Titan–Hyperion	0.1042	–

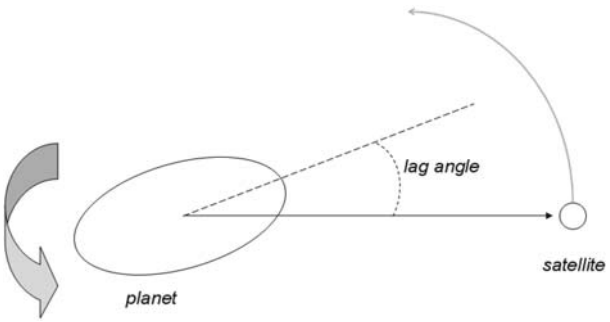

Fig. 1 Tidal bulges configuration induced by a tide raising satellite on its primary, assuming a faster rate for the planet spin than the satellite mean motion

the satellite. In the following we assume prograde motion of the satellite (Triton's retrograde orbit is the only exception). If the satellite revolves slower than the planet rotates—which is the case for all large and medium-sized satellites—, the tidal bulge of the planet will be ahead of the sub-planet line (see Fig. 1). The torque exerted by the satellite on the planet's tidal bulge will cause the planet to rotate slower, while conservation of angular momentum will increase the satellite's semi-major axis. On the other hand, if the satellite revolves faster than the planet rotates—which is the case for Phobos and also for several small inner satellites of the giant planets—, the satellite will cause the planet rotation rate to increase while the satellite's orbit will regress.

Under the assumption of low eccentricity, low inclination and outside of resonance we have (Goldreich and Soter 1966)

$$\frac{da}{dt} = +3\left(\frac{k_2}{Q}\right)_p \frac{m_s}{m_p}\left(\frac{R_p}{a}\right)^5 na, \quad \text{and} \tag{13}$$

$$\frac{de}{dt} = +\frac{57}{8}\left(\frac{k_2}{Q}\right)_p \frac{m_s}{m_p}\left(\frac{R_p}{a}\right)^5 ne. \tag{14}$$

Here t is the time, m the mass, k_2 the second-degree potential Love number, Q the quality factor, R the radius, and p and s denote parameters referring to the planet and the satellite, respectively.

3.2.2 Tides Raised in the Satellite

Synchronous Spin-Orbit Resonance The rotation rate of most of the natural satellites has slowly evolved to an equilibrium state as a result of tidal dissipation in the satellites' interiors. In equilibrium, the satellites rotate synchronously with their orbital motion, meaning that they have on average (see above) equal rotation and revolution periods.

Satellite tides are caused by the gravitational field of a planet, which periodically deforms the natural satellites orbiting the planet. Since friction is associated with tidal deformation, tidal energy is converted to heat and the tides lag in phase with respect to the driving force (as for a damped forced oscillator). As a result, the tidal bulge of the satellite is misaligned with respect to the line joining the mass centers of the satellite and the planet. For a zero-obliquity satellite in a circular equatorial orbit, the tidal torque Γ on the satellite as a result of the misaligned tidal bulge can be written as (e.g. Goldreich 1963; MacDonald 1964; for the more general case of eccentric and inclined orbits, see Ferraz-Mello et al. 2008)

$$\Gamma = \frac{3}{2} k_2 \frac{G m_p^2}{R_s} \left(\frac{R_s}{a} \right)^6 \sin 2\epsilon. \tag{15}$$

Here, R_s is the mean radius of the satellite, a the semi-major axis of the satellite's orbit, k_2 the degree two potential Love number of the satellite, and ϵ the geometric phase lag between the tidal bulge and the planet-satellite line. The tidal torque changes the rotation rate Ω_s according to e.g. Peale (1999) (the second approximate identity is for a homogeneous body)

$$\frac{d\Omega_s}{dt} = -\frac{3}{2} \left(\frac{k_2}{Q} \right)_s \frac{G m_p^2 R_s^5}{C_s a^6} \text{sign}(\Omega_s - n) \approx -\frac{45}{76} \frac{\rho_s R_s^2}{\mu_s Q_s} n^4 \text{sign}(\Omega_s - n), \tag{16}$$

and the rotation angular velocity decreases in a despinning time scale τ given by

$$\tau \approx \frac{76}{45} \frac{\Omega_s \mu_s Q_s}{\rho_s R_s^2} \frac{1}{n^4} \text{sign}(\Omega_s - n). \tag{17}$$

Here, Q_s is the quality factor, C_s the polar moment of inertia, ρ_s the mean density, and μ_s the mean bulk modulus of the satellite. By taking typical values as $Q_s = 100$ and $\mu_s = 10^{10}$ Pa, this equation shows that the larger satellites despin in a short period compared to the age of the Solar System (e.g. Peale 1977). Values for τ are given in Table 8. A notable exception is the distant Iapetus, whose despinning time-scale is of the order of the age of the solar system.

Because of the strong distance dependence of the tidal torque, satellites despin more slowly with increasing distance from their central planet. Therefore, distant small satellites have almost retained their primordial spin up to the present time.

The final equilibrium rotation state for a spherically symmetric satellite is the synchronous rotation for a circular orbit but has a rotation rate slightly faster than synchronous for an eccentric orbit (we neglect obliquity here) due to the larger accelerating effect on rotation near pericenter than the decelerating effect near apocenter (see, e.g., Murray and Dermott 1999). Since despinning is the fastest tidally driven evolution, satellites still have an elliptical orbit upon reaching an equilibrium rotation state. The synchronous equilibrium state for

an eccentric orbit is stable if the torque of the central planet on a permanent asymmetry of the satellite is larger than the tidal torque at synchronous rotation averaged over an orbital period (Goldreich and Peale 1966), which can be expressed for the small eccentricities of the satellites as

$$C_{22} > 3e^2 \left(\frac{k_2}{Q}\right)_s \frac{m_p}{m_s} \left(\frac{R_s}{a}\right)^3 \approx \frac{9}{19} \frac{\rho_s R_s^2}{\mu_s Q_s} n^2 e^2. \tag{18}$$

Here a constant tidal lag is assumed. Other tidal lag models can lead to a different dependency on e (e.g., Greenberg and Weidenschilling 1984). All large and medium-sized (radius > 200 km) satellites are synchronous rotators. Equation (18) shows that relaxed satellites in hydrostatic equilibrium have a sufficiently large C_{22}, typically of the order of 10^{-3} to 10^{-5}, for the synchronous rotation state to be stable. However, since the direction of the long axis of a satellite differs slightly from the direction to the central planet at pericenter due to the balance between the tidal torque and the torque on the asymmetry for synchronous rotation, the satellite's figure will tend to change slowly by creep to adapt to the tidal potential. To maintain the equilibrium orientation, the satellite will rotate slightly asynchronously (Greenberg and Weidenschilling 1984; Ferraz-Mello et al. 2008). Evidence for non-synchronous rotation of Europa, which has been suggested by Greenberg and Weidenschilling (1984) and by Ojakangas and Stevenson (1989b) has been obtained based on analysis of surface features (Hoppa et al. 2001).

Orbital Variations As the main satellites of the giant planets are locked in a 1:1 spin orbit resonance, no exchange of angular momentum is expected from tidal effects. Nevertheless, if a satellite is on an eccentric orbit, it will still experience tidal dissipation as, first, the distance to the primary changes with time, and second, the revolution rate will be higher at periapsis than at apoapsis. These two effects give rise to radial and librational tides, and hence dissipation. As the energy source is the orbital energy (equal to $-Gm_p m_s/2a$), tidal dissipation decreases the satellite semi-major axis. Moreover, conservation of angular momentum $m_s n a^2 \sqrt{1-e^2}$ will tend to decrease the eccentricity. After some computations and based on the assumption of small eccentricity and absence of resonances, we obtain for the evolution of a and e (Goldreich and Soter 1966)

$$\frac{da}{dt} = -21 \left(\frac{k_2}{Q}\right)_s \frac{m_p}{m_s} \left(\frac{R_s}{a}\right)^5 nae^2, \quad \text{and} \tag{19}$$

$$\frac{de}{dt} = -\frac{21}{2} \left(\frac{k_2}{Q}\right)_s \frac{m_p}{m_s} \left(\frac{R_s}{a}\right)^5 ne. \tag{20}$$

As all major satellites of the giant planets evolve beyond the synchronous orbit (defined by the distance to the primary for which orbital period equals the rotation period of the planet), competition arises between tidal dissipation in the planet and in the satellite. The induced expansion or regression of the orbit will be the result of the two opposing effects.

These changes in mean distance to the planet and orbital eccentricity are important for the evolution of resonances and for the tidal heat production on long time-scales. The amount of energy dissipated in the satellite interiors will be discussed in Sect. 4.4.1.

3.3 Observed Tidal Accelerations

Since the satellite semi-major axis and mean motion are related by Kepler's third law $n^2 a^3 = G(m_s + m_p)$, tidal dissipation can, in principle, be observed from monitoring of the satellite orbits as a mean motion acceleration or deceleration.

Table 2 Selection of tidal secular accelerations for the Galilean satellites in the form $\dot{n}/n$ (units are in 10^{-10} yr^{-1})

Reference	Io	Europa	Ganymede
Lieske (1987)	-0.074 ± 0.087	-0.082 ± 0.097	-0.098 ± 0.153
Goldstein and Jacobs (1995)	$+4.54 \pm 0.95$	$+5.6 \pm 5.7$	$+2.8 \pm 2.0$
Vasundhara (1996)	$+2.27 \pm 0.70$	-0.67 ± 0.80	$+1.06 \pm 1.00$
Aksnes and Franklin (2001)	$+3.6 \pm 1.0$	–	–

3.3.1 The Galilean Satellite System

The first estimates of the secular tidal accelerations among the Galilean system have to be credited to De Sitter (1928). He derived a significant tidal acceleration for all three inner Galilean satellites (as they are locked in the Laplace resonance). Decades passed since new estimations were computed by different authors (see Table 2). Using an accurate orbital model first developed by Sampson (1921) and improved by Lieske (1977), Lieske (1987) derived secular accelerations from the use of old eclipses. He found no accelerations within the errors, which could suggest that the tides raised in Jupiter by the Galilean moons counterbalance the tides raised by Jupiter on Io. Using Sampson-Lieske's orbital theory with different observational sets, subsequent authors found discordant results (i.e., Vasundhara et al. 1996 and Aksnes and Franklin 2001).

Comparing Sampson-Lieske theory to numerical simulation, Avdyushev (2004) and Lainey et al. (2004) showed that the internal precision of Sampson-Lieske theory was of the order of a few hundred of kilometers. Such lack of precision compared to the tidal acceleration effect was unexpected and attributed to the lack of long period terms in the model. This probably explains the disagreement in the quantification of orbital accelerations from astrometry in the past. Using a full numerical model to compute the orbital evolution of the Galilean system, Lainey et al. (2009) considerably improved the internal accuracy on the satellite positions at the level of few hundred of meters, only. Moreover, tidal accelerations were not derived from a quadratic fit on astrometric residuals, but obtained directly as a consequence of modeling the lag of the tidal potential in the dynamics. This allowed the authors to obtain independently the tidal dissipation in both Io and Jupiter. Considering a set of astrometric observations covering the period (1891–2007) (and neglecting over such a short time span the influence of tidal dissipation in Europa and Ganymede on the Galilean orbits), they found $(k_2/Q)_{\mathrm{Io}} = 0.015 \pm 0.003$ and $(k_2/Q)_{\mathrm{J}} = (1.102 \pm 0.203) \times 10^{-5}$ for Io and Jupiter, respectively.

Since the three innermost Galilean moons are locked in the Laplace resonance, strong correlations arise when dissipation is considered in Europa or Ganymede. Hence, this method may not provide strong constraints for tidal dissipation in Europa, unless tidal dissipation in Io is fixed. Using very precise gravity field determinations and altimetry an orbiter around Europa may provide better options to derive Europa's rate of dissipation by detecting the lag angle of the tidal response. Alternatively, a radio beacon at the surface might be able to transmit the tidal signal with sufficient accuracy. Both methods are technically challenging, mainly because of the harsh radiation environment at Europa and the resulting relatively short duration of measurements.

3.3.2 The Saturnian System

Mimas is the only Saturnian satellite that has been suspected to accelerate when comparing its expected position from orbital model to astrometric observations. An anomalous acceleration of about 2° cy^{-2} was found successively by Kozai (1957) and Dourneau (1987). A few years after Dourneau's result, Vienne et al. (1992) using a more accurate orbital theory of the Saturnian satellites proved that the anomalous acceleration of Mimas was most probably a long-period term that was missing in the former orbital models. No other accelerations have been reported recently among the Saturnian system.

4 Energy Sources

Many different forms of energy play a role in the evolution of satellites. However, their significance may vary considerably for individual objects and with time. In the following, the energy sources and their corresponding internal heat production, the main driver for internal processes, are described.

4.1 Nuclear Energy

Nuclear energy can be released by the decay of unstable isotopes in the rock component of planets and satellites. The energy available due to the mass defect is—apart from the small amount of neutrino energy—eventually converted into heat within the rocky material. Whereas radioactive isotopes of uranium, thorium, and potassium (Table 3) with half-lives of the order of 10^9 years are important throughout the evolution, three isotopes—^{26}Al, ^{60}Fe, and ^{53}Mn—having half-lives of the order of million years, can be relevant during the satellites' accretion and possibly during the very early stages of evolution. With the given mass m_{sil} of the silicate component of a specific satellite the total time dependent heat production rate $\dot{E}_{\mathrm{rad}}$ due to long-lived radioactive isotopes in watts is calculated from

$$\dot{E}_{\mathrm{rad}} = m_{\mathrm{sil}} \sum_{i=1}^{4} c_i C_i H_i \exp\left[\lambda_i (t - t_{\mathrm{pr}})\right], \tag{21}$$

where i stands for the four long-lived isotopes. C is the abundance of uranium, thorium, potassium typical for a specific class of meteorites and has to be assumed according to Tables 4 or 5. From the half-lives (Table 3) the decay constants can be calculated by $\lambda_i = \ln 0.5/\tau_i$. t is the time variable, starting with $t = 0$ at the time of the satellites' formation and $t_{\mathrm{pr}} = 4.6 \times 10^9$ yr is the present time. In Fig. 2 the total heat production rate per unit mass, $\dot{E}_{\mathrm{rad}}/m_{\mathrm{sil}}$ is shown as a function of time for selected types of meteorites. Variation due to the different elemental abundances can reach a factor of about 1.7 with the ordinary LL chondrites (high) and the carbonaceous CI chondrites (low) being the most extreme cases. Representative present-day heat production rates per unit mass are about 3.45 pW kg^{-1} (CI), 4.55 pW kg^{-1} (EH), 5.20 pW kg^{-1} (CO), and 5.75 pW kg^{-1} (LL). The obtained present-day total heat production rates of the satellites, accounting for the silicate mass fraction, are summarized in Table 6.

Table 3 Half-lives τ, present (for long-lived isotopes) and initial (for short-lived isotopes) composition c, and heat release H for long-lived isotopes and—separated by a horizontal line—short-lived isotopes (Audi et al. 1997; Lodders and Fegley 1998; Spohn 1997; Castillo-Rogez et al. 2007)

i	Isotope	τ, years	c, kg kg^{-1}	H, W kg^{-1}
1	^{238}U	4.468×10^9	0.992745	9.48×10^{-5}
2	^{235}U	0.7038×10^9	7.2×10^{-3}	5.69×10^{-4}
3	^{232}Th	14.05×10^9	1.0	2.69×10^{-5}
4	^{40}K	1.277×10^9	1.17×10^{-4}	2.92×10^{-5}
5	^{26}Al	0.740×10^6	^{26}Al/^{27}Al $= 5 \times 10^{-5}$	0.146
6	^{60}Fe	1.5×10^6	^{60}Fe/^{56}Fe $= 0.1$–1×10^{-6}	0.068–0.074
7	^{53}Mn	3.74×10^6	^{53}Mn/^{55}Mn $= 1$–4×10^{-5}	0.027

Table 4 Elemental abundance of radionuclides and densities of carbonaceous chondrites (Lodders and Fegley 1998)

i	Element	CI	CM	CV	CO	CK	CR	CH
1,2	U, ppb	8	12	17	18	15	13	
3	Th, ppb	29	41	58	80	58	42	
4	K, ppm	550	370	360	360	290	315	200
5	Al, wt.%	0.865	1.13	1.68	1.40	1.47	1.15	1.05
6	Fe, wt.%	18.2	21.3	23.5	25.0	23.0	23.8	38.0
7	Mn, ppm	1940	1650	1520	1620	1440	1660	1020
	ρ, kg m^{-3}	2230	2710	3420	3630	3400	3270	4200

Table 5 Elemental abundance of radionuclides and densities of ordinary and enstatite chondrites (Lodders and Fegley 1998)

i	Element	H	L	LL	R	Acap.	K	EH	EL
1,2	U, ppb	13	15	15	<25			9.2	7.0
3	Th, ppb	38	42	47	<50			30	38
4	K, ppm	780	920	880	780	475	710	840	700
5	Al, wt.%	1.06	1.16	1.18	1.06	1.2	1.3	0.82	1.00
6	Fe, wt.%	27.2	21.75	19.8	24.4	23.5	24.7	30.5	24.8
7	Mn, ppm	2340	2590	2600	2960	3000	2400	2120	1580
	ρ, kg m^{-3}	3800	3600	3550	3600	3700	3700	3670	3580

4.2 Potential Energy

The potential energy U of a radially symmetric mass distribution $M(r)$ is obtained by integrating $-(GM(r)/r)dm$ over all mass elements dm or, equivalently, over the volume V if the density distribution is given:

$$U = -\int_V \frac{GM(r)}{r}\rho(r)dV. \tag{22}$$

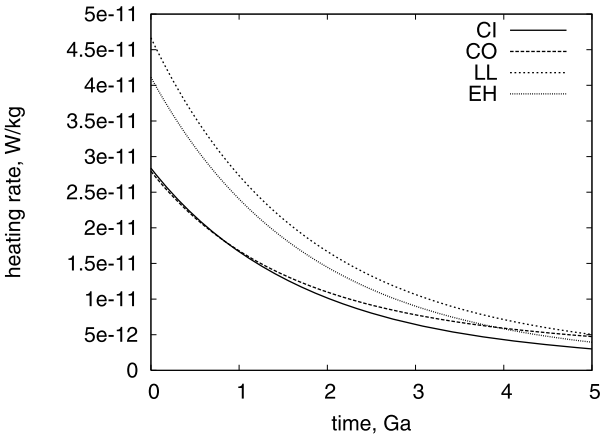

Fig. 2 Specific heat production rates due to long-lived isotopes for different classes of meteorites (Carbonaceous CI and CO-chondrites, ordinary LL-chondrites and enstatite EH-chondrites) as a function of time. Present-day values are obtained after 4.6 Ga

Table 6 Rock-mass fraction $M_{\rm rock}$ (including metal) and heat production rates $\dot{E}_{\rm rad}$ due to long-lived isotopes for the largest satellites. Io's density of about 3529 kg m^{-3} is assumed as a typical value for the density of rock. The ranges correspond to the heat production rates assuming a CI and LL-chondritic composition, respectively. Other types of chondrites range between these two. In case of Io, the CI-chondrite would be inconsistent with the satellite's mean density. Numbers are given for the initial (t_0) and present-day ($t_{\rm pr}$) heating rates, respectively

Satellite	$M_{\rm rock}$, wt.%	$\dot{E}_{\rm rad}(t_0)$, W	$\dot{E}_{\rm rad}(t_0)/V$, W m^{-3}	$\dot{E}_{\rm rad}(t_{\rm pr})$, W	$\dot{E}_{\rm rad}(t_{\rm pr})/V$, W m^{-3}
Io	100	$(2.50–4.15)\times10^{12}$	$\sim 1.31\times10^{-7}$	$(3.08–5.14)\times10^{11}$	$\sim 1.62\times10^{-8}$
Europa	92	$(1.24–2.05)\times10^{12}$	$\sim 1.03\times10^{-7}$	$(1.52–2.54)\times10^{11}$	$\sim 1.27\times10^{-8}$
Ganymede	67	$(2.78–4.62)\times10^{12}$	$\sim 4.84\times10^{-8}$	$(3.43–5.71)\times10^{11}$	$\sim 5.98\times10^{-9}$
Callisto	64	$(1.93–3.20)\times10^{12}$	$\sim 4.38\times10^{-8}$	$(2.38–3.96)\times10^{11}$	$\sim 5.41\times10^{-9}$
Mimas	18	$(1.92–3.18)\times10^{8}$	$\sim 7.81\times10^{-9}$	$(2.36–3.93)\times10^{7}$	$\sim 9.65\times10^{-10}$
Enceladus	53	$(1.63–2.71)\times10^{9}$	$\sim 3.24\times10^{-8}$	$(2.01–3.35)\times10^{8}$	$\sim 4.00\times10^{-9}$
Tethys	<0.1	$(1.04–1.73)\times10^{7}$	$\sim 2.18\times10^{-11}$	$(1.28–2.14)\times10^{6}$	$\sim 2.70\times10^{-12}$
Dione	45	$(1.39–2.30)\times10^{10}$	$\sim 2.48\times10^{-8}$	$(1.71–2.85)\times10^{9}$	$\sim 3.07\times10^{-9}$
Rhea	27	$(1.75–2.90)\times10^{10}$	$\sim 1.24\times10^{-8}$	$(2.15–3.59)\times10^{9}$	$\sim 1.53\times10^{-9}$
Titan	65	$(2.45–4.07)\times10^{12}$	$\sim 4.56\times10^{-8}$	$(3.02–5.03)\times10^{11}$	$\sim 5.63\times10^{-9}$
Iapetus	12	$(0.61–1.01)\times10^{10}$	$\sim 4.85\times10^{-9}$	$(0.75–1.25)\times10^{9}$	$\sim 5.99\times10^{-10}$
Miranda	23	$(4.25–7.06)\times10^{8}$	$\sim 1.03\times10^{-8}$	$(5.24–8.73)\times10^{7}$	$\sim 1.27\times10^{-9}$
Ariel	56	$(2.12–3.52)\times10^{10}$	$\sim 3.47\times10^{-8}$	$(2.61–4.35)\times10^{9}$	$\sim 4.28\times10^{-9}$
Umbriel	40	$(1.31–2.18)\times10^{10}$	$\sim 2.08\times10^{-8}$	$(1.61–2.69)\times10^{9}$	$\sim 2.57\times10^{-9}$
Titania	58	$(5.73–9.52)\times10^{10}$	$\sim 3.71\times10^{-8}$	$(0.71–1.18)\times10^{10}$	$\sim 4.58\times10^{-9}$
Oberon	54	$(4.55–7.56)\times10^{10}$	$\sim 3.27\times10^{-8}$	$(5.61–9.35)\times10^{9}$	$\sim 4.04\times10^{-9}$
Triton	72	$(4.31–7.16)\times10^{11}$	$\sim 5.54\times10^{-8}$	$(5.32–8.86)\times10^{10}$	$\sim 6.84\times10^{-9}$
Charon	60	$(2.72–4.52)\times10^{10}$	$\sim 3.90\times10^{-8}$	$(3.35–5.59)\times10^{9}$	$\sim 4.82\times10^{-9}$

Here, $G = 6.67259 \times 10^{-11}\ \mathrm{m^3\,kg^{-1}\,s^{-2}}$ is the gravitational constant, r the distance from the center of mass, and ρ the density. For a homogeneous ($\rho = \text{const.}$) sphere with radius R, and by using spherical coordinates and $M(r) = (4/3)\pi r^3 \rho$ we obtain

$$U_\mathrm{h} = -4\pi\rho \int_0^R \frac{GM}{r} r^2 dr = -\frac{16}{3}\pi^2\rho^2 G \int_0^R r^4 dr = -\frac{16}{15}\pi^2\rho^2 G R^5 = -\frac{3GM^2}{5R}. \quad (23)$$

Accretion The formation of satellites by accretion of smaller bodies releases gravitational energy. If a homogeneous satellite is assumed as an end-state of the accretional processes, Equation (23) provides the total amount of potential energy available in the satellite. However, the satellite's state after accretion may also be non-homogeneous. The energy per unit mass released during accretion is thus parameterized by

$$E_\mathrm{ac} = \chi GM/R, \quad (24)$$

where χ is a factor of order unity accounting for different accretion processes (Schubert et al. 1986). In case of a homogeneous end-state $\chi = 3/5$. In that case all the energy released due to later differentiation will be available in the satellite's interior. In general, however, part of this energy will heat the satellite's interior while the other part is radiated into space. The latter fraction is not well-constrained and the amount of heat released during accretion is uncertain. In contrast to later stages of evolution the near-surface temperature is high compared to the temperature in the deep interior during and shortly after accretion (Schubert et al. 1986).

Differentiation Energy of differentiation will be released by core formation and/or the separation of other distinct layers which differ in density (e.g., HP-ice, liquid water, ice-I). For the two-layer case (core radius and density R_1 and ρ_1, respectively; mantle radius $R_2 = R$ and density ρ_2, respectively) the total potential energy U_d is that of the core (23)

$$U_1 = -\frac{16}{15}\pi^2\rho_1^2 G R_1^5, \quad (25)$$

plus that of the spherical mantle shell. The latter is—analogous to the integration above (22)—given by

$$U_2 = -\frac{16}{3}\pi^2 G \left(\frac{\rho_1\rho_2 R_1^3}{2}(R_2^2 - R_1^2) + \frac{\rho_2^2}{5}(R_2^5 - R_1^5) - \frac{\rho_2^2 R_1^3}{2}(R_2^2 - R_1^2) \right). \quad (26)$$

The mass distribution is in this case given by $M(r) = 4/3\pi\rho_1 r^3$ for $0 \le r \le R_1$, and $M(r) = 4/3\pi(\rho_1 R_1^3 + \rho_2(r^3 - R_1^3))$ for $R_1 \le r \le R_2$. The potential energy of a two-layer satellite is then given by $U_\mathrm{d} = U_1 + U_2$. The energy released by transition from the homogeneous to the completely differentiated two-layer state is thus given by

$$U_\mathrm{pot} = U_\mathrm{h} - U_\mathrm{d} = -\frac{16}{15}\pi^2\rho^2 G R_2^5 - (U_1 + U_2), \quad (27)$$

where $\rho = 3M/(4\pi R_2^3)$ is the mean density of the satellite with total mass M.

In Table 7 the potential energies for homogeneous and two-layer differentiated satellites are compared. The differentiated states assume densities of 1000 and 3500 $\mathrm{kg\,m^{-3}}$ for the outer ice-layer and rock-core, respectively. Exceptions are Io (3275 and 5150 $\mathrm{kg\,m^{-3}}$), the large icy satellites—Ganymede, Callisto and Titan—for which we assume an ice density of

Table 7 Potential energy U_h and U_d for the homogeneous (23) and the two-layer differentiated (27) case. The heating rate due to differentiation $\dot{E}_{diff}$ is estimated assuming a time scale of 100 Myr

Satellite	U_h, J	U_d, J	$\dot{E}_{diff}$, W	$\dot{E}_{diff}/V$, W m^{-3}
Io	1.75×10^{29}	1.81×10^{29}	1.70×10^{12}	6.72×10^{-8}
Europa	5.91×10^{28}	6.35×10^{28}	1.41×10^{12}	8.85×10^{-8}
Ganymede	3.34×10^{29}	4.66×10^{29}	4.20×10^{13}	5.50×10^{-7}
Callisto	1.92×10^{29}	2.05×10^{29}	3.89×10^{12}	6.64×10^{-8}
Mimas	2.92×10^{23}	3.04×10^{23}	3.97×10^{6}	1.22×10^{-10}
Enceladus	1.92×10^{24}	2.11×10^{24}	5.92×10^{7}	8.82×10^{-10}
Tethys	2.89×10^{25}	2.91×10^{25}	5.43×10^{7}	8.56×10^{-11}
Dione	8.62×10^{25}	9.66×10^{25}	3.27×10^{9}	4.40×10^{-9}
Rhea	2.80×10^{26}	2.89×10^{26}	3.00×10^{9}	1.61×10^{-9}
Titan	2.81×10^{29}	3.06×10^{29}	7.85×10^{12}	1.10×10^{-7}
Iapetus	1.78×10^{26}	1.88×10^{26}	3.15×10^{9}	1.89×10^{-9}
Miranda	7.40×10^{23}	8.04×10^{23}	2.05×10^{7}	3.73×10^{-10}
Ariel	1.26×10^{26}	1.45×10^{26}	6.01×10^{9}	7.40×10^{-9}
Umbriel	9.37×10^{25}	1.06×10^{26}	3.97×10^{9}	4.75×10^{-9}
Titania	6.32×10^{26}	7.35×10^{26}	3.24×10^{10}	1.58×10^{-8}
Oberon	4.76×10^{26}	4.50×10^{26}	2.33×10^{10}	1.26×10^{-8}
Triton	1.36×10^{28}	1.53×10^{28}	5.65×10^{11}	5.45×10^{-8}
Charon	1.74×10^{26}	2.02×10^{26}	9.11×10^{9}	9.82×10^{-9}

1300 kg m^{-3}, Rhea (1000 and 1465 kg m^{-3}) and Tethys (quasi homogeneous assuming 917 and 1000 kg m^{-3}). In cases where there are constraints available for the moment of inertia values—Io, Europa, Ganymede, Callisto, Rhea—these are matched by adjusting the core sizes accordingly. This procedure fails for Ganymede which at present is highly differentiated and cannot be described by a two-layer model. For Ganymede and also for Europa and other satellites, which presumably are further differentiated into three or more layers this estimate may thus represent an earlier stage of evolution.

4.3 Kinetic Energy

Kinetic energy plays a major role in many processes inside icy moons. In the early stages of evolution the kinetic energy of impactors is converted into heat. The resulting (near-) surface temperature is much higher as compared to the internal temperature in this phase. This changes when the radiogenic heating from the deep interior becomes the dominant heat source after accretion has ceased.

Flows of material—be it solid ice and rock or liquid water—transport heat by convection from the interior to the surface. In the case of electrically conducting material these processes can generate magnetic fields. The intrinsic field of Ganymede, generated in the satellite's liquid iron core, is an important example of such motion on macroscopic scales in satellite interiors.

4.3.1 Rotation

A satellite's energy of rotation is given by

$$E_{\mathrm{rot}} = \frac{1}{2} C_s \Omega^2 = \frac{1}{5} m_s R_s^2 \Omega^2, \tag{28}$$

where C_s is the polar moment of inertia and Ω the rotation rate. At the right hand side the homogeneous case $C_s = 2/5 m_s R_s^2$ has been assumed. In that approximation the rate of energy change is given by

$$\dot{E}_{\mathrm{rot}} = \frac{2}{5} m_s R_s^2 \Omega \dot{\Omega}. \tag{29}$$

After accretion, the rotation rates of the satellites are decreasing due to tidal dissipation in the satellites' interiors. Assuming an initial rotation period of, e.g. 10 h, the timescales for despinning can be calculated from (16). The results for the despinning timescales and the corresponding heating rates are shown in Table 8. The initial rotation period is unknown and the dissipative response (k_2/Q) may not be constant. However, the values show that despinning to the synchronous state can significantly contribute to the energy budget of satellites early in their histories. The volumetric heating rates are high especially for Io, Europa, Ganymede, Tethys, Ariel and Triton. An extreme case is Iapetus where the heating rates are very small and the despinning timescale is of the order of the age of the solar system, presumably indicating that Iapetus' k_2/Q (time averaged) was lower (for details, see Schubert et al. 2010, this issue).

4.4 Energy of Deformation

As discussed above, satellites are distorted mainly due to rotation and due to external forces, i.e. tides. Whereas the former changes only on very long-timescales and leads to a quasi-static deformation, the frequency of the forcing for satellite tides is of the order of days or weeks. This can cause dynamical deformations of the satellite that are—depending on the planetary material and the frequency of the forcing—partly elastic (energy conserved) and partly inelastic (dissipation of energy). Internal friction involved with the latter can significantly contribute to the energy balance of satellites, that are on eccentric orbits, close to their primary planets. In the following we will discuss the relevance of inelastic tidal deformation of the solid part (mainly ice and rock) of a satellite for internal processes. Tyler (2008) has suggested that substantial dissipation within an ocean on Europa can occur due to the resonant excitation of Rossby waves. However, in the following we will focus on solid-body tides, only.

4.4.1 Inelastic Deformation: Tidal Dissipation Processes in Icy Moons

Most of the icy moons are subjected to a periodic variation of gravitational forces along their orbit about their central planet, owing to the orbital eccentricity. The materials that compose the moon's interior deform according to these periodic force variations. For a layered satellite, the response of each internal layer is determined by the thermo-mechanical properties of the dominating material (e.g., liquid iron/iron sulfide for the core, olivine for the silicate mantle, liquid water for the ocean, high-pressure phase layer and hexagonal ice-I for the icy shells). Owing to the anelastic properties of the materials in their interiors, part of the energy involved in the tidal deformation is dissipated into heat. As detailed below,

Table 8 Despinning time-scales τ (17), despinning heating rates $\dot{E}_{\rm rot}$ assuming an initial period of 10 h, volumetric despinning heating rate $\dot{E}_{\rm rot}/V$, present-day tidal heating rate $\dot{E}_{\rm sync}$ in synchronous rotation and present-day volumetric tidal heating rate $\dot{E}_{\rm sync}/V$ of the largest satellites. Homogeneous density distributions and for $\dot{E}_{\rm sync}$ Maxwell rheologies are assumed. For the rocky moons (only Io and Europa) and for the icy moons elastic rigidities of $\mu = 65$ GPa and $\mu = 3.5$ GPa, respectively, are assumed. For the viscosity we use 10^{16} Pa s and 10^{15} Pa s for rock and ice, respectively. Such low rock-viscosities are applicable only for 'Io-like' partially molten rock which is assumed here also for Europa. Furthermore, the entire volume of the satellite is assumed to dissipate. The obtained dissipation rates should therefore be regarded as possible maximum values

Satellite	τ, yr	$\dot{E}_{\rm rot}$, W	$\dot{E}_{\rm rot}/V$, W m^{-3}	$\dot{E}_{\rm sync}$, W	$\dot{E}_{\rm sync}/V$, W m^{-3}
Io	1400	3.9×10^{16}	1.53×10^{-3}	2.7×10^{13}	1.1×10^{-6}
Europa	42,000	5.4×10^{14}	3.36×10^{-5}	2.5×10^{12}	1.6×10^{-7}
Ganymede	21,000	9.2×10^{15}	1.20×10^{-4}	2.8×10^{11}	3.6×10^{-9}
Callisto	830,000	1.5×10^{14}	2.48×10^{-6}	1.6×10^{11}	2.7×10^{-9}
Mimas	1100	2.1×10^{11}	6.34×10^{-6}	1.5×10^{9}	4.7×10^{-8}
Enceladus	2750	4.5×10^{11}	6.63×10^{-6}	2.1×10^{8}	3.1×10^{-9}
Tethys	4200	7.8×10^{12}	1.22×10^{-5}	1.8×10^{6}	2.8×10^{-12}
Dione	12,000	5.5×10^{12}	7.41×10^{-6}	6.4×10^{8}	8.6×10^{-10}
Rhea	61,000	4.2×10^{12}	2.25×10^{-6}	1.1×10^{8}	5.7×10^{-11}
Titan	591,000	2.9×10^{14}	4.07×10^{-6}	4.5×10^{12}	6.3×10^{-8}
Iapetus	7.8×10^{9}	2.4×10^{7}	1.44×10^{-11}	5.3×10^{5}	3.2×10^{-13}
Miranda	4900	1.3×10^{11}	2.40×10^{-6}	4.8×10^{6}	8.8×10^{-11}
Ariel	7100	1.2×10^{13}	1.48×10^{-5}	4.1×10^{8}	5.1×10^{-10}
Umbriel	65,000	1.2×10^{12}	1.41×10^{-6}	4.5×10^{8}	5.4×10^{-10}
Titania	599,000	7.1×10^{11}	3.44×10^{-7}	2.2×10^{7}	1.1×10^{-11}
Oberon	3.9×10^{6}	8.5×10^{10}	4.62×10^{-8}	4.4×10^{6}	2.4×10^{-12}
Triton	34,300	2.2×10^{14}	2.12×10^{-5}	1.3×10^{7}	2.4×10^{-12}
Charon	284,000	4.0×10^{11}	4.32×10^{-7}	5.0×10^{7}	5.4×10^{-11}

several kinds of dissipation processes can occur within a satellite. The total energy that can be generated by these dissipation processes depend on both the orbital configuration and the mechanical properties of each internal layer. In some circumstances, the tide-generated energy can exceed all the other sources of energy and induce a thermal runaway.

Viscous friction in convective layers Each layer that composes the satellite's interior deforms differently depending on its viscoelastic properties. The amplitude of deformation in liquid layers (liquid metallic core or water ocean) is large as there is little resistance to shear motions except at boundary layers. In contrast, the deformation of cold rigid lithosphere is small as they possess a high resistance to shear motions. In the liquid case, the tidal motion is large, but as the resistance is extremely low, little viscous dissipation occurs. In the rigid case, the resistance is so large that viscous motions are prohibited, and the deformation is only determined by the elastic properties of the layer. Anelastic deformation can contribute to the total motion, but only if the solid material has sufficient time to deform as a viscous body. This can occur for forcing periods close and beyond the Maxwell time, which is the ratio between the viscosity of the materials and the rigidity.

The global tidal heating rate in synchronous rotation on a slightly eccentric orbit $\dot{E}_{\rm sync}$ can be calculated by (Segatz et al. 1988)

$$\dot{E}_{\rm sync} = -\frac{21 R_s^5 n^5 e^2}{2G} \mathrm{Im}(k_2), \tag{30}$$

where besides previously defined quantities, $\mathrm{Im}(k_2)$ is the imaginary part of the second degree potential Love number. This formulation is independent of specific rheology. However, to calculate $\mathrm{Im}(k_2)$ assumptions as to the rheological model (e.g., Maxwell or alternative models) and on the density distribution of the satellite are required. Assuming a Maxwell body the rigidity μ_c is a complex number with real and imaginary part given by

$$\mathrm{Re}(\mu_c) = \eta^2 n^2 \mu / (\mu^2 + \eta^2 n^2) \quad \text{and} \quad \mathrm{Im}(\mu_c) = \eta n \mu^2 / (\mu^2 + \eta^2 n^2), \tag{31}$$

where μ and η are the elastic rigidity, and the viscosity of the body, respectively. In the homogeneous case the complex degree-two Love number is given by

$$k_2 = 1.5 / \left(1 + \frac{19}{2} \frac{\mu_c}{\rho g R_s}\right), \tag{32}$$

where g is the gravitational acceleration at the surface. The factor $3/2$ is the Love number in the fluid limit. Tidal heating rates for the homogeneous case can thus be obtained from (30) by inserting (32). Results for the major satellites are summarized in Table 8. Because of the approximations (homogeneous satellite) these are only very rough estimates of the tidal heating rates. The real values can be considerably lower especially for larger viscosities (as is the case for many icy satellites, e.g. for Mimas) or if the dissipating volume is only a small fraction of the satellite. Additionally, the presence of liquid layers would enhance the deformation of the overlying shells significantly. Nevertheless, the estimates are useful to generally compare possible maximum tidal heating rates.

On microscopic scales, the viscous mechanisms are mainly related to the motions of defects and their interaction with the crystal lattice, resulting in friction. During the first quarter of a tidal cycle, strain energy is progressively stored as compressive (or tensile) stress increases. During the second quarter, strain energy is restored as stress decreases. The same process operates during the other half period when stress is tensile (or compressive). The back-and-forth motions of crystal defects (or atomic and molecular diffusion) induced by alternating compression and tension convert part of the strain energy into heat. The efficiency of such dissipative processes depends on the population of existing defects (or dislocations) and therefore is very sensitive to the density of existing dislocations within the crystal lattice (e.g. Cole et al. 1998). From a macroscopic point of view, the anelastic behavior of a material sample results in a time delay of the material response relative to tidal forcing, in a smaller effective shear modulus and in the production of heat. As the mobility of crystal defects is strongly temperature-dependent, the amount of dissipated energy at a given frequency strongly varies within a convective layer, which may be characterized by strong lateral and radial temperature contrast. Different models are proposed in the literature to describe the temperature dependence of dissipation processes. The Maxwell model is classically used to describe the viscoelastic response of both ice and silicate mantles (e.g. Ojakangas and Stevenson 1989a; Sohl et al. 1995; Hussmann et al. 2002; Moore 2003; Tobie et al. 2005a). It is adapted to describe material relaxation properties when the forcing period is close to their Maxwell time, but it fails to quantify dissipation processes over a wide range of frequencies and temperature (Sotin

et al. 2009). Other models, based on laboratory measurements (e.g., Tatibouet et al. 1986; Cole 1995 on cyclic loading) or geophysical measurements (e.g., Reeh et al. 2003 on tidal bending of polar glaciers) are probably more appropriate for describing the viscoelastic response over a wide range of temperature (see also Durham et al. 2010, this issue). Whatever the rheological models, significant viscous dissipation is expected to occur within convective mantles for temperature ranging between 200–270 K for icy mantles and 1000–1600 K for silicate mantles.

Even if viscous dissipation in a water ocean might be negligible, the presence of an ocean strongly increases the deformation amplitude of the above ice shell, and hence the amount of dissipated energy. In a convective ice shell on Europa, owing to the decoupling effect of the ocean, the tidal heating rate can reach values between 10^{-6} and 10^{-5} W m^{-3}, which is more than one hundred times the volumetric radiogenic heating rate in the silicate mantle (e.g. Tobie et al. 2003). The dissipation rate could vary by one order of magnitude between cold and hot plumes, and the localization of maximum heating rate (in hot or cold plumes) is very sensitive to the rheological parameters (Tobie et al. 2003; Mitri and Showman 2005). On Enceladus, the viscous dissipation rate at the south pole can reach values of the order of 10^{-7} and 10^{-6} W m^{-3} if an internal ocean is present (Tobie et al. 2008). On Titan, solid tidal dissipation is expected to be much smaller (Sohl et al. 1995), but may still reach values comparable to radiogenic heating (of the order of 10^{-8} W m^{-3}) (Tobie et al. 2005b). On Io, the dissipation rate in the silicate mantle must reach values of at least 10^{-5} W m^{-3} in order to explain the observed surface heat flow (Segatz et al. 1988). On Europa, the dissipation rate in the silicate mantle is highly uncertain, but could reach values of roughly 10^{-7} W m^{-3} if the mantle is as hot and dissipative as Io's mantle (see also Moore and Hussmann 2009).

Shear friction along faults Localized deformation along faults within the cold icy lithosphere can also provide a significant source of dissipation. This process may be important for satellites that exhibit large-scale faulting and are subjected to large tidal deformations (e.g. on Europa, on Enceladus, and possibly on Triton). By applying a shear deformation model initially developed for Earth applications (Yuen et al. 1978), Nimmo and Gaidos (2002) proposed that shear heating owing to tidally-induced strike-slip motion along fractures could locally raise the temperature, possibly up to the melting point at shallow depths. Dissipation in this model is also related to viscous deformation in the warmer part of the layer, but in this case, the rate of deformation is locally controlled by the displacements along the faults, which is very high near the faults. This model initially adapted to Europa has been more recently applied to Enceladus (Nimmo et al. 2007) and Triton (Prockter et al. 2005). If faults are subjected to large shear displacements (of the order of 0.1–0.5 m per day), the temperature could locally rise up to the melting point of water ice at the base of the faults. Such large shear velocities can occur only if the lithosphere is subjected to very large tidal deformations, implying the existence of a decoupling liquid layer a few tens of kilometers below the surface. In their model, Nimmo and Gaidos (2002) prescribed the displacement rate, independently of the amount of work that might be needed to create the shear motions. Preblich et al. (2007) and Smith-Konter and Pappalardo (2008) showed that tidal displacements along tectonic faults are smaller than initially anticipated by Nimmo and Gaidos (2002). This mainly follows from the fact that the shear velocity rates prescribed by Nimmo and Gaidos (2002) are valid for two sliding rigid blocks above a totally fluid layer. It does not take into account the resistance due to friction between the two rigid blocks and the resistance due to the viscous ice layer below, which would tend to reduce the shear motion rate. Despite these limitations, shear heating along tidally-forced faults remains a viable mechanism, but is probably overestimated in existing models. Further modeling efforts are required to better quantify this process.

4.5 Latent Heat and Chemical Energy

Phase Transitions Depending on internal temperature and pressure conditions the state of aggregation of the planetary material may change during satellite evolution. For icy satellites the crystallization of water and the associated release of latent heat is the most relevant process. To melt the mass m of ice, the latent heat of $\Delta H = Lm$ must be provided. $L = 334$ kJ/kg is the latent heat of fusion of water. Latent heat released by crystallization of liquid H_2O can significantly contribute to the internal energy budget. If we for instance assume an H_2O-layer thickness of Europa of 150 km, the latent heat released by solidification of the entire layer would amount to 1.4×10^{27} J. Assuming a timescale of 100 Myr this would imply a heating rate of 4.4×10^{11} W, comparable to the present radiogenic heating rate. With a larger amount of water the corresponding values for Ganymede are 1.80×10^{28} J and 5.69×10^{12} W. For likely situations in icy satellites the latent heat energy would be comparable to the product of heat capacity and the temperature change.

For large satellites which may contain liquid water layers, melting and freezing of water can be relevant for both the ocean floor, where high-pressure ices form and the top of the ocean where ice-I forms. Other phase transitions, e.g., the transition from one phase of high-pressure ice to another (depending on temperature) may release additional energy .

Exogenic Reactions Energy can be provided by chemical reactions. An important example for a possible reaction in icy satellites is the process of serpentinization (see also Sohl et al. 2010, this issue). Provided that liquid water is available in icy moons and that a rock-ocean interface exists, for instance on Europa, serpentine may be formed from olivine by rock-water interactions, e.g.

$$\text{forsterite} + \text{water} \leftrightarrow \text{brucite} + \text{serpentine}, \tag{33}$$

$$2Mg_2SiO_4 + 3H_2O \leftrightarrow Mg(OH)_2 + Mg_3Si_2O_5(OH)_4. \tag{34}$$

The serpentine-producing reaction is exogenic and provides an average enthalpy of $\Delta H = -83$ kJ per mole serpentine. The efficiency of the reaction will depend on temperature and pressure conditions and mainly on the percolation depth of the water into the rock. The latter can be estimated by applying a model of micro-cracking to the rock-layer of the icy satellites at the specific temperature and pressure conditions. Vance et al. (2007) have found that the heat flux due to serpentinization is of the order of 1% of the heat flux due to radiogenic heating. However, it may be significant especially for small icy moons where the percolation depth is greater (as compared to large icy moons) because of the smaller pressures. Cracks can penetrate deeper and the rock-volume available for the above reaction is correspondingly larger. For a completely differentiated Enceladus, for instance, the cracking-depth could reach down to the center of the moon. This could imply around 6% of heating due to serpentinization as compared to radiogenic heating, i.e. a quite significant contribution (Vance et al. 2007), if the core was initially ultramafic.

5 Heat Transfer in Icy Moons

Heat within a satellite interior is mainly transported by thermal diffusion and thermal convection. In the present section, we present the basic concepts of thermal diffusion and thermal convection and discuss the conditions for which each of these two processes is predominant in the context of icy moons. In addition to thermal diffusion and convection, vapor

and/or cryomagma emission can also significantly contribute to the heat transfer at shallow depths, in some particular circumstances. These specific processes are discussed in more detail in other contributions of this volume and will not be further detailed here. Finally, coupling between tidal heating and heat transfer is also a key process in icy moons.

5.1 Conductive Transfer Within Icy Moons

Thermal conduction is the dominant mechanism for heat transport where the viscosity is large enough to inhibit the initiation of convective motions. Under these conditions, the efficiency of heat transfer is mainly controlled by the thermal conductivity and heat capacity of the materials in the satellites' interiors.

Such stable conditions are reached in the smallest satellites, which remain cold during their entire history. Similar conditions are also reached within the inner part of mid-sized and large satellites just after the accretion: owing to the deposition of accretional energy, the outer part of a satellite is warmer than the inner part just after the accretion whereas the center has a low temperature (e.g. Schubert et al. 1986). As this kind of thermal structure is stable against thermal convection, heat transfer is dominated by conduction alone during the early stage of the satellite evolution. Finally, the upper part of the outer icy layer remains cold during most of the evolution, even on the largest satellites, and internal heat is mainly transferred through thermal diffusion toward the surface.

5.1.1 Thermal Diffusion in a Cold Ice-Rock Core

The conductive transfer of energy in a cold core consisting of a mixture of rock and ices can be described by the following time-dependent heat conduction equation for radial symmetry, where all materials parameters may be functions of temperature and pressure (e.g., Hillier and Squyres 1991):

$$\rho c_p \frac{\partial T}{\partial t} = \frac{k}{r}\frac{\partial^2 (rT)}{\partial r^2} + \frac{\partial k}{\partial r}\frac{\partial T}{\partial r} + \rho H(t,r), \tag{35}$$

where t is time, k is thermal conductivity, ρ is density, c_p is heat capacity, and $H(t,r)$ is the rate of heat production per unit mass.

For any initial temperature profile and any surface temperature, the above equation can be easily solved provided that conductivity, heat capacity, density and heating profiles are prescribed. For a mixture of silicate and ices, thermal conductivity and heat capacity can be estimated from the volume and mass fraction of each phase:

$$k = f_s k_s + (1 - f_s) k_i, \tag{36}$$

$$c_p = x_s c_{p,s} + (1 - x_s) c_{p,i}, \tag{37}$$

where f_s and x_s are the silicate volume and mass fraction of the mixture, respectively. Whereas (37) is exact, it should be noted that (36) is valid only for rock and ice units (layers) aligned in parallel to the direction of heat flow. Heat sources includes radioactive decay of isotopes in the silicate phase, tidal friction in the whole mixture, and possibly phase changes.

During the early stage of evolution, the excess energy deposited in the outer region during accretion is diffused toward the surface, resulting in a progressive cooling of the outer layer. In the inner portion, as thermal diffusion is not very efficient, the heat produced by radioactive decay cannot be entirely evacuated and the interior progressively warms up. At

some point, as discussed in the next section, thermal convection can initiate or the melting point of ice can be reached. In this latter condition, a rapid differentiation of the interior can occur. For the smallest satellites, a temperature warm enough to initiate convection or to melt the interior is never reached, except if a significant amount of short-lived isotopes was initially present (e.g., Castillo-Rogez et al. 2007).

For the largest satellites, a segregation of rock and ice is very likely to occur, thus leading to the formation of a discrete rock core. A full segregation would result from a relatively hot start of the satellite involving melting of the ice component (e.g., Kirk and Stevenson 1987 in the case of Ganymede). Another mechanism may be a gradual but incomplete solid-state differentiation of the ice-rock mixture (e.g., Nagel et al. 2004 for Callisto). Just after differentiation, the temperature in the core is also too low to permit convective motions of rock. Heat is transferred by conduction only and the evolution of the temperature profile can be determined by (35) by setting a rock mass fraction of 1. As the rocky core is relatively cold during this diffusive stage, heating by tidal friction is negligible.

Although only the time integration of (35) can provide the exact solution of the conductive evolution of the core, an approximate solution can also be derived by assuming an initially isothermal core. Assuming that there is no conductive heat loss, the increase in core temperature as a function of time can be estimated from the rate of radiogenic heating $H_{0,i}e^{-\lambda_i t}$ for each unstable isotope (e.g., Kirk and Stevenson 1987; Grasset et al. 2000):

$$\Delta T_c(t) = \frac{1}{c_{p,c}} \sum_i H_{0,i} \frac{1 - e^{-\lambda_i t}}{\lambda_i}. \tag{38}$$

In fact, part of the energy is lost by thermal diffusion through a boundary region of width $\sim (\kappa_c t)^{1/2}$, where $\kappa_c = k_c/(\rho_c c_{p,c})$ is the thermal diffusivity of the core. The diffusive heat flux across this boundary is:

$$F_c = \frac{2k_c \Delta T_c}{\sqrt{\pi \kappa_c t}}. \tag{39}$$

As this conductive heat flow remains small relative to the heat production, the core warms and subsolidus convection becomes eventually possible. In the case of Titan and Ganymede, this diffusive stage lasts about 1.5 to 2 billion years (Kirk and Stevenson 1987; Tobie et al. 2006). The duration of the diffusive stage in the rocky core is mainly determined by the initial content in radiogenic elements and the degree of hydration of the silicates, which strongly influence the rock viscosity and hence the onset of convection (Tobie et al. 2006, Fig. 3).

5.1.2 Thermal Diffusion Through an Icy Shell

Even for satellites with very warm interiors (e.g. Enceladus, Europa, Titan etc.), a significant part of the internal heat is transported by thermal conduction through the last kilometers below the surface. The evolution of the temperature profile in this upper layer can be calculated from (35) by imposing a constant temperature at the surface and the heat flux coming from the inner part at the base. The only source of heating is provided by tidal friction. As tidal energy is only efficiently converted into heat for ice having a temperature larger than 200 K, this source of energy is only located in the warmer part of the conductive layer, i.e. at its base (e.g. Ojakangas and Stevenson 1989a; McKinnon 1999). As this source of energy remains small, it has no major impact on the

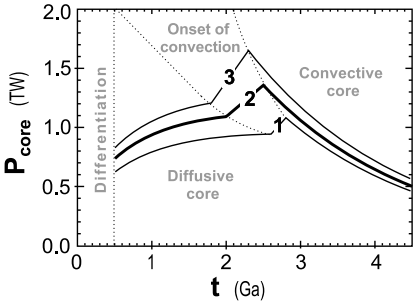

Fig. 3 Estimation of global heat power provided by the rocky core of Titan. Three different mineral compositions, reflecting different hydration states, have been used to estimate the possible evolution of the silicate core over a reasonable range: 1, $\rho_{\rm sil} = 3000$ kg m^{-3}, $H_0 = 3 \times 10^{-11}$ W kg^{-1}, $T_i = 1400$ K; 2, $\rho_{\rm sil} = 3300$ kg m^{-3}, $H_0 = 4 \times 10^{-11}$ W kg^{-1}, $T_i = 1500$ K; 3, $\rho_{\rm sil} = 4000$ kg m^{-3}, $H_0 = 5 \times 10^{-11}$ W kg^{-1}, $T_i = 1600$ K, where $\rho_{\rm sil}$ is the silicate density, H_0 is the initial radiogenic heating rate and T_i is the interior temperature required to trigger thermal convection in the silicate core. Evolution of the silicate core is characterized by a diffusive stage following the differentiation and a convective stage once the interior is sufficiently hot. Depending on the composition of the silicate core, we estimate an onset time of convection of between 1.8 and 2.8 Gyr (from Tobie et al. 2006)

thermal structure of the conductive layer. Therefore, at equilibrium ($\partial T/\partial t = 0$), the conductive heat flow across a layer of thickness d having a surface temperature of $T_{\rm surf}$ and a bottom temperature of $T_{\rm bot}$ is described by a simple Fourier law:

$$\phi_{\rm cond} = k \frac{T_{\rm surf} - T_{\rm bot}}{d}. \tag{40}$$

However, owing to a significant temperature dependence ($k(T) = 488.12/T\,({\rm K}) + 0.4685$), the thermal conductivity of water ice is expected to vary from 2–2.5 W m^{-1} K^{-1} near the melting point to more than 5 W m^{-1} K^{-1} at a temperature of 100 K. Due to this effect, heat is more efficiently transferred at shallow depths where temperature increases more slowly with depth whereas temperature gradients are larger at deeper levels. As a consequence, for an equivalent heat flow and for a bottom temperature of 220–240 K (Tobie et al. 2003), the thickness between the surface and the bottom is 1.5 to 2 times larger if the temperature dependence of thermal conductivity is considered.

Other factors may also influence the thermal conductivity of an icy layer. The presence of other compounds with a lower conductivity, such as gas clathrates, ammonia hydrates, salts (e.g., Ross and Kargel 1998) can significantly reduce the effective thermal conductivity of the layer. On Titan, for instance, the presence of methane clathrate in large quantities is expected to strongly influence the cooling rate of the whole satellite (Tobie et al. 2006). On Europa also, various gas clathrates, if present, are expected to modify the thermal structure of the shell (e.g., Prieto-Ballesteros et al. 2005). The thermal conductivity is also expected to be reduced if the upper part of the icy layer includes a significant porous fraction (e.g., Eluszkiewicz 1990; Leliwa-Kopystyński and Kossacki 2000). As ice resists compaction at low temperature, a significant porosity can be preserved during a very long period of time and hence influence the thermal evolution of the satellite, in particular on small and cold bodies (Eluszkiewicz 1990).

Finally, the presence of significant tidal dissipation at the base of conductive layer (e.g. Ojakangas and Stevenson 1989a; Tobie et al. 2003) can reduce the heat flow across a conductive layer just above a liquid water ocean and hence limits the crystallization rate of

the liquid layer. On Europa, a thermal equilibrium is reached for a tidally-heated conductive layer having a thickness of 25–30 km (e.g. Ojakangas and Stevenson 1989a). However, as it is discussed below, when an icy shell reaches such a thickness, thermal convection is expected to occur.

5.2 Onset of Convection and Convective Transfer

Convective motion can be initiated within the solid-state interior of a satellite due to the potentially unstable top-heavy configuration induced by the conjunction of a temperature field hotter in the inner part of the satellite and of a positive thermal expansivity α. In his seminal paper (see Strutt 1916), Lord Rayleigh demonstrated in the simple framework of a plane fluid layer heated from below, that the occurrence of such convective instabilities is dictated by the value of the non-dimensional parameter Ra,

$$\mathrm{Ra} = \frac{\alpha \rho g \Delta T d^3}{\kappa \eta}, \tag{41}$$

measuring the relative contribution of buoyancy forces ($\alpha \rho g \Delta T$, with g gravity and, $\Delta T = T_{\mathrm{bot}} - T_{\mathrm{surf}}$, the temperature difference across the layer) to the factor inhibiting fluid motion, i.e., viscosity η.

5.2.1 Basic Equations of Thermal Convection

The equations describing thermal convection in an incompressible fluid correspond to the three conservation equations for mass, momentum and energy,

$$\nabla \cdot \mathbf{V} = \mathbf{0}, \tag{42}$$

$$\rho \left(\frac{\partial V}{\partial t} + \mathbf{V} \cdot \nabla \mathbf{V} \right) = -\nabla \mathbf{p} + \nabla \cdot \tau + \mathbf{f}, \tag{43}$$

$$\rho c_p \left(\frac{\partial T}{\partial t} + \mathbf{V} \cdot \nabla T \right) = k \nabla^2 T + \rho H. \tag{44}$$

with the notations introduced earlier. The velocity ($\mathbf{V}$) and pressure (p) fields describe the flow induced by the buoyancy force ($\mathbf{f} = \rho(T)\mathbf{g}$) given that a viscous rheology is introduced that relates the strain rate tensor ($(\nabla \mathbf{V}) + ^t (\nabla \mathbf{V})$) to the deviatoric stress tensor τ. The above formulation results from the hypothesis that thermodynamical coefficients (such as α, κ, ...) vary only by very moderate amounts so that they can be neglected as well as variations of ρ, except in the buoyancy term that drives convection (*Boussinesq approximation*). As indicated above, this assumption is only partly valid for satellites' interiors, especially for icy layers.

In addition, conservation of momentum (or *Navier-Stokes equation* (43)) is often simplified as, for icy or rocky materials, the value of the diffusivity of momentum (or kinematic viscosity η/ρ) is extremely large when compared to the thermal diffusivity κ (*infinite Prandtl number approximation*). As a consequence, inertial terms in the left hand side of (43) are neglected and the time evolution of the system resides entirely in the conservation of energy (44).

In the context of satellites, as indicated above, the "fluid" layer models either a sphere (corrresponding to a global undifferentiated interior or solely to the silicate core) or a spherical shell (corrresponding, for example, to an icy layer). Solid state creep of icy or rocky

materials enables the description of long term motion with viscous fluid dynamics. A major characteristic is that the effective viscosity associated with these thermally activated processes varies strongly with temperature. Typically, the temperature differences ΔT associated with internal layers of icy satellites lead to several orders of magnitude variations for the viscosity of these materials, ices or rocks.

As a consequence, one specificity of thermal convection within icy satellites is that these solid state dynamics, if they operate, often occur in the so called *stagnant lid regime* obtained asymptotically for very large viscosity contrasts. In this case, as mentioned in the previous section, convective flow develops only in the warmer part of the layer, beneath a cold conductive lid. Since most of the viscosity variations occur within this lid, heat transfer in the convective sublayer below can be described as isoviscous convection (e.g., Solomatov 1995; Grasset and Parmentier 1998). Equation (44) is a generalized version of (35) when convection occurs: it indicates the dual nature of convective transfer where both conduction ($k\nabla^2 T$), as described in Sect. 5.1 of this paper, and advection (transfer associated to flow, $\rho c_p \mathbf{V}\cdot\nabla T$) coexist. Usually, advection is dominant in the bulk of the layer and diffusion becomes larger in regions near the boundaries (*thermal boundary layers*).

5.2.2 *Conditions for Initiating Convection*

The evaluation of the Rayleigh number Ra (according to (41)) should be sufficient to decide whether convective instabilities initiate or not in a (given layer of a) given satellite, if the simple isoviscous fluid, plane layer approximation is valid—the critical value of Ra is about 1000; even when the more realistic geometries of a sphere or a spherical shell are introduced, the linear stability analysis provides similar orders of magnitudes (Chandrasekhar 1961). If all icy satellites are considered as undifferentiated mixtures of ices and rocks, variations in values of κ and α are probably not significant when evaluating the order of magnitude of the Rayleigh number for a given satellite. Neither are the variations in mean density among satellites (so that g can also be approximated by a linear function of the satellite's radius R_s) or the global temperature difference potentially driving convection. Reasonable values for these parameters lead to $\mathrm{Ra} \simeq (R_s^4/\eta)$. However, unfortunately, due to a very large range of possible values for the reference viscosity η (induced by the nature of the creeping material and its temperature, mostly), the plausible range for Ra generally forbids a definitive conclusion.

The criterion for the onset of convection has been studied in the context of fluids with strongly temperature-dependent viscosity (e.g. Stengel et al. 1982): additional complexities arise when considering that the rheology of ices and rocks may also depend on stress, grain size and pressure. At large grain sizes and/or high temperatures, for example, materials flow by strongly stress-dependent dislocation creep. The onset of convection for such a viscosity, $\eta \sim \tau^{n-1}$ (with n, stress exponent), is then a highly non-linear problem addressed by only few studies (e.g. Solomatov and Barr 2006).

The critical value of Ra is often considered as a mean to investigate whether convection instabilities will develop in the outer icy shell of large Galilean satellites and eventually what is the depth of plausible internal oceans. The existence of such deep oceans is supported by electromagnetic induction signatures for Europa (Kivelson et al. 2000) and Callisto (Zimmer et al. 2000). The magnetic field data returned by several flybys of Ganymede is also interpreted in terms of a layer of liquid water at depth (Kivelson et al. 2002). While the evaluation of the critical thickness for convection to occur in the outer icy crust is addressed by many authors assuming a Newtonian rheology for the ice I shell (generally leading to values of a few tens of kilometers), the consideration of a more complex rheology demonstrates the

important role of the grain size distribution and initial thermal state (Barr and Pappalardo 2005).

While the above problem of the stability of an icy layer can be interesting in terms of the present-day internal structure of satellites, a different approach is to consider the following transient problem: given that the interior is potentially heated uniformly (this would be the case for a silicate core or an ice/rock mixture, see (38)) and cannot lose enough heat by conduction alone (39), what is the critical time for convection to occur? In this case, the first instabilities take place where the largest temperature gradient is present, for example, beneath the boundary region near the surface of the core, mentioned in the previous section. In the isoviscous framework, it has been shown that the onset time for this transient problem can again be related to a critical value of the local Rayleigh number defined using the depth $\sim (\kappa t)^{1/2}$ of the cold front rather than the whole thickness of the layer Howard (1964). In the stagnant lid regime, only the fraction of this cold boundary layer where viscosity η_c is sufficiently low to participate to convective motion should be considered (e.g. Kirk and Stevenson 1987). The local Rayleigh number can then be approximated by

$$\mathrm{Ra}_\delta(t) = \frac{\alpha \rho g \Delta T_c(t) (\kappa t)^{3/2}}{\kappa \eta_c(t)}. \tag{45}$$

5.2.3 *Efficiency of Heat Transfer*

Once convection is initiated, a measure of the efficiency of heat transfer is provided by the Nusselt number Nu. This second dimensionless parameter is defined as the ratio between the surface heat flux ϕ induced by the convective transfer and the conductive heat flux (ϕ_{cond}, (40)) that would be obtained for the same layer if advective motions were not present. Scaling relationships of the form

$$\mathrm{Nu} \sim \mathrm{Ra}^{\beta} \tag{46}$$

are obtained for various convective set-ups: for isoviscous fluids, values of $\beta \simeq -1/3$ are generally reported. Since real configurations may imply both basal and internal heating, a potentially important effect is the precise distribution of mixed heat sources (Sotin and Labrosse 1999; Moore 2008; Choblet and Parmentier 2009). Departures from this simple framework are thus plausible.

A parameterized evolution of the satellite's interior can then be considered, following the method first proposed for terrestrial planets by Schubert et al. (1979): assuming steady-state heat transfer, the global heat balance for the internal spherical shell between radii R_{bot} and R_{top} results from the integration of (44),

$$\rho c_p \frac{\partial T}{\partial t} = \rho H + 3 \frac{\phi_{\mathrm{top}} R_{\mathrm{top}}^2 - \phi_{\mathrm{bot}} R_{\mathrm{bot}}^2}{R_{\mathrm{top}}^3 - R_{\mathrm{bot}}^3}, \tag{47}$$

the values of fluxes ϕ being associated to the convective vigor of the layer through (46).

The value of the exponent β is naturally modified in the context of the stagnant lid regime that inhibits the efficiency of heat transfer when such an insulating viscous layer forms on top of the convective region (appropriate values of β are thus smaller, cf. for example Solomatov 1995). Applications to the outer shell of large icy satellites at present-day are specifically proposed by Deschamps and Sotin (2001) indicating the role of convective heat transfer on the possible radial structures of these objects (preservation or complete crystallization of a residual internal ocean). Thermal evolutions of the Galilean satellites

(Spohn and Schubert 2003), Titan (Tobie et al. 2006) or smaller mid-sized icy satellites of Saturn (Multhaup and Spohn 2007) are based on a similar conceptual framework. These studies indicate that specific parameters attributable to each of these bodies may induce different evolutionary paths. One such factor is the amount of ammonia in the water-ice system that largely affects the phase diagram (e.g. Sotin et al. 1998). Methane clathrates possibly controlling the coupled evolution of the interior and atmospheric processes are also likely candidates.

The general cases discussed here are the basis for more complex models in which different aspects of satellite evolution must be combined. The history of tidal heating induced by the orbital evolution of some of the satellites, implies that in some cases coupled methods (internal dynamics, shape relaxation, orbital evolution) are required to properly describe their evolution.

6 Concluding Remarks

In this chapter we have discussed the main energy sources which drive processes in the satellites' interiors. Furthermore, we have described the rotational and orbital states, which are closely linked to the internal energy budget by tidal friction. Depending on the size, different rock mass fraction, internal composition, and interaction with other satellites and the primary planet through tides and resonances, the relevance of these energy sources may strongly vary for different objects. Furthermore, there can be strong variations with time. E.g., whereas tidal friction plays a major role as a heat source on Io and Enceladus, such processes can at present be neglected for most of the satellites. Tidal despinning, however, may have been an important process involving dissipation of heat for all major satellites early in their histories. The conversion of different energy contributions into heat and the transport of the latter triggers processes, which are very diverse for the individual satellites. Such processes and their relevance for the evolution of satellites are discussed in other contributions to this volume. Examples are the interaction of thermal convection and despinning of Iapetus, the melting induced by tidal heating in plumes in convecting satellites, the chemical cycles on Titan, serpentinization and ocean chemistry on Europa, or localized heating in the ice shell of Enceladus.

To combine the effects relevant for the evolution of specific satellites is a challenging task. *Cassini* and *Galileo* data as well as ground-based astrometry of satellite orbits and laboratory studies on ices are major tools to improve our current models on satellite evolution. Furthermore, such tools are essential for the preparation of the future exploration of the outer planets and their moons.

Acknowledgements We would like to thank W.B. McKinnon and an anonymous reviewer for the very helpful and constructive comments.

Part of this work was carried out at the Jet Propulsion Laboratory, California Institute of Technology, under contract with NASA. Part of this work has been supported by the Helmholtz Association through the alliance 'Planetary Evolution and Life'.

References

K. Aksnes, F.A. Franklin, Astron. J. **122**, 2734–2739 (2001)
G. Audi, O. Bersillon, J. Blachot, A.H. Wapstra, Nucl. Phys. A **624**, 1–124 (1997)
V.A. Avdyushev, Sol. Syst. Res. **38**, 238–240 (2004)
A.C. Barr, R.T. Pappalardo, J. Geophys. Res. **110**, E12 (2005). CiteID E12005

R.H. Brown, T.V. Johnson, R.L. Kirk, L.A. Soderblom, Science **250**, 431–435 (1990)
J.C. Castillo-Rogez, D.L. Matson, C. Sotin, T.V. Johnson, J.I. Lunine, P.C. Thomas, Icarus **190**, 179–202 (2007)
A. Cayley, Mem. R. Astron. Soc. **29**, 191–306 (1861)
S. Chandrasekhar, *Hydrodynamic and Hydromagnetic Stability*. International Series of Monographs on Physics (Clarendon, Oxford, 1961)
G. Choblet, E.M. Parmentier, Phys. Earth Planet. Inter. **173**, 290–296 (2009)
D.M. Cole, Philos. Mag. A **72**, 231–248 (1995)
D.M. Cole, R.A. Johnson, G.D. Durell, J. Geophys. Res. **103**(C10), 21751–21758 (1998)
R.L. Comstock, B.G. Bills, J. Geophys. Res. **108**(E9), 5100 (2003). doi:10.1029/2003JE00210
W. De Sitter, Leiden Ann. **16**(2), 1–92 (1928)
F. Deschamps, C. Sotin, J. Geophys. Res. **106**, 5107–5121 (2001)
G. Dourneau, Thesis, Bordeaux, 1987
W.B. Durham, O. Prieto-Ballesteros, D.L. Goldsby, J.S. Kargel, Space Sci. Rev. (2010, this issue). doi:10.1007/s11214-009-9619-1
D.H. Eckhardt, Moon Planets **25**, 3–49 (1981)
J. Eluszkiewicz, Icarus **84**, 215–225 (1990)
S. Ferraz-Mello, A. Rodriguez, H. Hussmann, Celest. Mech. Dyn. Astron. **101**, 171–201 (2008)
P.E. Geissler, Annu. Rev. Earth Planet. Sci. **31**, 175–211 (2003)
P. Goldreich, Mon. Not. R. Astron. Soc. **126**, 257–268 (1963)
P. Goldreich, S.J. Peale, Astron. J. **71**, 425–437 (1966)
P. Goldreich, S. Soter, Icarus **5**, 375–389 (1966)
O. Grasset, E.M. Parmentier, J. Geophys. Res. **103**, 18171–18181 (1998)
O. Grasset, C. Sotin, F. Deschamps, Planet. Space Sci. **48**, 617–636 (2000)
R. Greenberg, S.J. Weidenschilling, Icarus **58**, 186–196 (1984)
J. Hillier, S.W. Squyres, J. Geophys. Res. **96**, 15665–15674 (1991)
G.V. Hoppa, B.R. Tufts, R. Greenberg, T.A. Hurford, D.P. O'Brien, P.E. Geissler, Icarus **153**, 208–213 (2001)
L.N. Howard, in *Proceedings of the Eleventh International Congress of Applied Mechanics*, vol. 153, ed. by H. Gortler (Springer, New York, 1964), pp. 1109–1115
W.B. Hubbard, *Planetary Interiors* (Van Nostrand Reinhold, New York, 1984)
H. Hussmann, T. Spohn, K. Wieczerkowski, Icarus **156**, 143–151 (2002)
H. Jeffreys, *The Earth. Its Origin, History and Physical Constitution* (Cambridge University Press, Cambridge, 1952)
Ö. Karatekin, T. Van Hoolst, T. Tokano, Geophys. Res. Lett. **35**, L16202 (2008). doi:10.1029/2008GL034744
R.L. Kirk, D.J. Stevenson, Icarus **69**, 91–134 (1987)
M.G. Kivelson, K.K. Khurana, C.T. Russell, M. Volwerk, R.J. Walker, C. Zimmer, Science **289**, 1340–1343 (2000)
M.G. Kivelson, K.K. Khurana, M. Volwerk, Icarus **157**, 507–522 (2002)
Y. Kozai, Ann. Tokyo Astron. Obs. **73**, 1 (1957)
V. Lainey, L. Duriez, A. Vienne, Astron. Astrophys. **420**, 1171–1183 (2004)
V. Lainey, L. Duriez, A. Vienne, Astron. Astrophys. **456**, 783–788 (2006)
V. Lainey, J.E. Arlot, O. Karatekin, T. Van Hoolst, Nature **459**, 957–959 (2009)
J. Leliwa-Kopystyński, K.J. Kossacki, Planet. Space Sci. **48**, 727–745 (2000)
J.H. Lieske, Astron. Astrophys. **176**, 146–158 (1987)
J.H. Lieske, Astron. Astrophys. **56**, 333–352 (1977)
K. Lodders, B. Fegley Jr., *The Planetary Scientists Companion* (Oxford Univ. Press, New York, 1998)
G.J.F. MacDonald, Rev. Geophys. Space Phys. **2**, 467–541 (1964)
F. Marchis et al., Icarus **176**, 96–122 (2005)
A.S. McEwen, L.P. Keszthelyi, R. Lopes, P.M. Schenk, J.R. Spencer, in *Jupiter: The Planet, Satellites, and Magnetosphere*, ed. by F. Bagenal, T.E. Dowling, W.B. McKinnon (Cambridge Univ. Press, Cambridge, 2004), pp. 307–328
W.B. McKinnon, in *Solar System Ices*, ed. by B. Schmitt, C. de Bergh, M. Festou (Kluwer, Dordrecht, 1998), p. 525
W.B. McKinnon, Geophys. Res. Lett. **26**, 951–954 (1999)
G. Mitri, A.P. Showman, Icarus **195**, 757–764 (2005)
W.B. Moore, J. Geophys. Res. **108**, E8 (2003). doi:10.1029/2002JE001943
W.B. Moore, J. Geophys. Res. **113**, B11407 (2008). doi:10.1029/2006JB004778
W.B. Moore, H. Hussmann, in *Europa*, ed. by R.T. Pappalardo, W.B. McKinnon, K.K. Khurana (University of Arizona Press, Tucson, 2009), pp. 369–380
H. Moritz, *The Figure of the Earth* (Herbert Wichmann, Karlsruhe, 1990)

K. Multhaup, T. Spohn, Icarus **186**, 420–435 (2007)
C.D. Murray, S.F. Dermott, *Solar System Dynamics* (Cambridge University Press, Cambridge, 1999)
K. Nagel, D. Breuer, T. Spohn, Icarus **169**, 402–412 (2004)
D.B. Nash, M.H. Carr, J. Gradie, D.M. Hunten, C.F. Yoder, in *Satellites*, ed. by J.A. Burns, M.S. Matthews (Univ. of Arizona Press, Tucson, 1986), pp. 629–688,
F. Nimmo, E. Gaidos, J. Geophys. Res. **107**, E4 (2002). doi:10.1029/2000JE001476
F. Nimmo, J.R. Spencer, R.T. Pappalardo, M.E. Mullen, Nature **447**, 289–291 (2007)
B. Noyelles, Celest. Mech. Dyn. Astron. **101**, 13–30 (2008)
G.W. Ojakangas, D.J. Stevenson, Icarus **81**, 220–241 (1989a)
G.W. Ojakangas, D.J. Stevenson, Icarus **81**, 242–270 (1989b)
J. Palguta, G. Schubert, K. Zhang, J.D. Anderson, Icarus **201**, 615–625 (2009)
S.J. Peale, in *Planetary Satellites*, ed. by J.A. Burns (Univ. of Arizona Press, Tucson, 1977), pp. 87–111
S.J. Peale, in *Satellites*, ed. by J.A. Burns, M.S. Matthews (Univ. of Arizona Press, Tucson, 1986), pp. 159–223
S.J. Peale, Annu. Rev. Astron. Astrophys. **37**, 533–602 (1999)
S.J. Peale, M.H. Lee, Science **298**, 593–597 (2002)
S.J. Peale, P. Cassen, R.T. Reynolds, Science **203**, 892–894 (1979)
C.C. Porco et al., Science **311**, 1393–1401 (2006)
B. Preblich, R. Greenberg, J. Riley, D. O'Brien, Planet. Space Sci. **55**, 1225–1245 (2007)
O. Prieto-Ballesteros, J.S. Kargel, M. Fernández-Sampedro, F. Selsis, E.S. Martínez, D.L. Hogenboom, Icarus **177**, 491–505 (2005)
L. Prockter, F. Nimmo, R.T. Pappalardo, Geophys. Res. Lett. **32**, 14 (2005). CiteID L14202
N. Reeh, E. Lintz Christensen, C. Mayer, O. Olesen, Ann. Glaciol. **37**, 83–89 (2003)
R.G. Ross, J.S. Kargel, in *Solar System Ices*, ed. by B. Schmitt, C. de Bergh, M. Festou (Kluwer, Dordrecht, 1998), p. 33
R.A. Sampson, Mem. R. Astron. Soc. **63**, 1–270 (1921)
G. Schubert, P. Cassen, R.E. Young, Icarus **38**, 192–211 (1979)
G. Schubert, T. Spohn, R.T. Reynolds, in *Satellites*, ed. by J.A. Burns, M.S. Matthews (Univ. of Arizona Press, Tucson, 1986), pp. 224–292
G. Schubert, J.D. Anderson, T. Spohn, W.B. McKinnon, in *Jupiter: The Planet, Satellites, and Magnetosphere*, ed. by F. Bagenal, T. Dowling, W.B. McKinnon (Cambridge Univ. Press, Cambridge, 2004), pp. 281–306
G. Schubert, H. Hussmann, V. Lainey, D. Matson, W.B. McKinnon, F. Sohl, C. Sotin, G. Tobie, D. Turrini, T. Van Hoolst, Space Sci. Rev. (2010, this issue)
M. Segatz, T. Spohn, M.N. Ross, G. Schubert, Icarus **75**, 187–206 (1988)
B.A. Smith et al., Science **204**, 951–957 (1979)
B. Smith-Konter, R.T. Pappalardo, Icarus **198**, 435–451 (2008)
L.A. Soderblom, T.L. Becker, S.W. Kieffer, R.H. Brown, C.J. Hansen, T.V. Johnson, Science **250**, 410–415 (1990)
F. Sohl, W.D. Sears, R.D. Lorenz, Icarus **115**, 278–294 (1995)
F. Sohl, H. Hussmann, B. Schwentker, T. Spohn, R.D. Lorenz, J. Geophys. Res. **108**, 5130 (2003)
F. Sohl, M. Choukroun, J. Kargel, J. Kimura, R.T. Pappalardo, S. Vance, M. Zolotov, Space Sci. Rev. (2010, this issue)
V.S. Solomatov, Phys. Fluids **7**, 266–274 (1995)
V.S. Solomatov, A.C. Barr, Phys. Earth Planet. Inter. **155**, 140–145 (2006)
C. Sotin, S. Labrosse, Phys. Earth Planet. Inter. **112**, 171–190 (1999)
C. Sotin, O. Grasset, S. Beauchesne, in *Solar System Ices*, ed. by B. Schmitt, C. de Bergh, M. Festou (Kluwer, Dordrecht, 1998), pp. 79–96
C. Sotin, G. Tobie, J. Wahr, W.B. McKinnon, in *Europa*, ed. by R.T. Pappalardo, W.B. McKinnon, K.K. Khurana (University of Arizona Press, Tucson, 2009), pp. 85–118
J.R. Spencer, J.C. Pearl, M. Segura, F.M. Flasar, A. Mamoutkine, P. Romani, B.J. Buratti, A.R. Hendrix, L.J. Spilker, R.M.C. Lopes, Science **311**, 1401–1405 (2006)
J.R. Spencer et al., Science **318**, 240 (2007)
T. Spohn, in *Bergmann, Schaefer: Lehrbuch der Experimentalphysik, Band 7: Erde und Planeten*, ed. by W. Raith (1997), pp. 427–525
T. Spohn, G. Schubert, Icarus **161**, 456–467 (2003)
K.C. Stengel, D.C. Oliver, J.R. Booker, J. Fluid Mech. **120**, 411–431 (1982)
B.W. Stiles, et al., Astron. J. **135**(5), 1669–1680 (2008). doi:10.1088/0004-6256/135/5/1669
B.W. Stiles et al. (the Cassini Radar Team), Astron. J. **139**, 311 (2010)
J.W. Strutt, Philos. Mag. **32**, 529–546 (1916)
J. Tatibouet, J. Perez, R. Vassoille, J. Phys. **47**, 51–60 (1986)

P.C. Thomas et al., Icarus **190**, 573–584 (2007)
G. Tobie, G. Choblet, C. Sotin, J. Geophys. Res. **108**, E11 (2003). doi:10.1029/2003JE002099
G. Tobie, A. Mocquet, C. Sotin, Icarus **177**, 534–549 (2005a)
G. Tobie, O. Grasset, J.I. Lunine, A. Mocquet, C. Sotin, Icarus **175**, 496–502 (2005b)
G. Tobie, J.I. Lunine, C. Sotin, Nature **440**, 61–64 (2006)
G. Tobie, O. Čadek, C. Sotin, Icarus **196**, 642–652 (2008)
T. Tokano, F.M. Neubauer, Geophys. Res. Lett. **32**, L24203 (2005)
R. Tyler, Nature **456**, 770–772 (2008)
T. Van Hoolst, N. Rambaux, Ö. Karatekin, V. Dehant, A. Rivoldini, Icarus **195**, 386–399 (2008). doi:10.1016/j.icarus.2007.12.011
T. Van Hoolst, Ö. Karatekin, in *European Planetary Science Congress 2008*. Extended abstract, 2008
T. Van Hoolst, N. Rambaux, Ö. Karatekin, Icarus **200**, 256–264 (2009). doi:10.1016/j.icarus.2008.11.009
S. Vance, J. Harnmeijer, J. Kimura, H. Hussmann, B. DeMartin, J.M. Brown, Astrobiology **7**, 987–1005 (2007)
R. Vasundhara, J.-E. Arlot, P. Descamps, in *Dynamics, Ephemerides, and Astrometry of the Solar System: Proceedings of the 172nd Symposium of the International Astronomical Union*, Held in Paris, France, 38 July 1995, ed. by S. Ferraz-Mello, B. Morando, J.-E. Arlot (1996), p. 145
A. Vienne, J.M. Sarlat, L. Duriez, in *Chaos, Resonance, and Collective Dynamical Phenomena in the Solar System: Proceedings of the 152nd Symposium of the International Astronomical Union*, ed. by S. Ferraz-Mello, Angra dos Reis, Brazil, 15–19 July 1991 (Kluwer Academic, Dordrecht, 1992), p. 219
J. Wisdom, Astron. J. **128**, 484–491 (2004)
F.E. Witteborn, J.D. Bregman, J.B. Pollack, Science **203**, 643–646 (1979)
C.F. Yoder, Nature **279**, 767–770 (1979)
D.A. Yuen, L. Fleitout, G. Schubert, C. Froidevaux, Int. J. Geophys. **54**, 93–119 (1978)
C. Zimmer, K.K. Khurana, M.G. Kivelson, Icarus **147**, 329–347 (2000)